3D elastoplastic model for fine–grained gassy soil considering the gas–dependent yield surface shape and stress–dilatancy

Yi Hong, Lizhong Wang*, Jianfeng Zhang and Zhiwei Gao

Abstract

Fine–grained sediments containing large discrete gas bubbles are widely distributed in the five continents throughout the world. The presence of gas bubbles could either degrade or enhance the hardening behaviour and undrained shear strength (s_{u}) of the soil, depending on the initial pore water pressure (u_{w0}) and initial gas volume fraction (ψ_0). The existing constitutive models, however, can solely capture either detrimental or beneficial effect owing to presence of gas. This study presents a new three–dimensional 3D elastoplastic constitutive model that describes both damaging and beneficial effects of gas bubbles on the stress–strain behaviour of fine–grained gassy soil in a unified manner. This was achieved by incorporating 1) a versatile expression of yield function that simulates a wide range of yield curve shapes in a unified context, and 2) a dilatancy function capturing the distinct stress–dilatancy behaviour of fine–grained gassy soil. Given the lack of direct experimental evidence on the shape of the yield curve of fine–grained gassy soil, new experiments were performed. This has led to the identification of three distinct shapes of bullet, ellipse, and teardrop as well as formulation of the yield function considering the dependency of yield curve shapes on u_{w0} and ψ_0. The new model was shown to reasonably capture both the damaging and beneficial effects of gas on the compression and shear behaviour of three types of fine–grained gassy soils with a broad range of u_{w0} and ψ_0 by using a unified set of parameters.

Author keywords: Constitutive modeling; Fine–grained gassy soil; Yield surface; Stress dilatancy; Critical state.

Introduction

Bubbles of undissolved gas, produced either biogenically or thermogenically, are widely present within shallow marine sediments throughout the five continents in the world (Grozic et al. 2000). Unlike the conventional unsaturated soils, the degree of saturation of fine–grained gassy marine sediments usually exceeds 85% (Sparks 1963; Nageswaran 1983), with a continuous water phase but a discontinuous phase of gas in discrete forms, as characterized by Hong et al. (2019a) using a micro–computed tomography (μCT) (Fig. 1(a)). The gas bubbles are significantly larger than the void spaces of the saturated soil matrix as shown in the scanning electron microscopy image in Fig. 1(b); thus, they cannot be treated as occluded bubbles that simply reduce the compressibility of the pore fluid (Wheeler 1988a, 1988b). Consequently, the large gas bubbles should have altered the structure of the soil to dramatically modify the mechanical behaviour of the soil (Wheeler 1988b; Lunne et al. 2001; Hight and Leroueil 2003; Puzrin et al. 2011; Rebata–Landa and Santamarina 2012; Sultan et al. 2012), with significant implications on the instability of offshore structures such as monopiles and pipelines and the occurrence of submarine landslides in gassy seabeds (Thomas et al. 2011; Kvenvolden 1988; Nisbet and Piper 1998; Milich 1999; Locat and Lee 2002; Kortekaas and Peuchen 2008; Dittrich et al. 2010; Evan 2011; Rowe and Mabrouk 2012; Xu et al. 2018).

The published experimental results (Wheeler 1988b; Hong et al. 2017) have suggested that the presence of gas bubbles could either degrade or enhance the hardening behaviour and undrained shear strength (s_{u}) of the soil, depending on the initial pore water pressure (u_{w0}) and initial gas volume fraction (ψ_0). On the other hand, the damaging and beneficial effects (s_{u} decreasing or increasing with ψ_0, respectively) due to presence of gas had been treated separately by the existing constitutive models for fine-grained gassy soil. Sultan and Garziglia (2014) proposed an anisotropic Cam Clay based constitutive model accounting for the damaging effect by gas. A new analytical expression that relates the preconsolidation pressure to a damage parameter depending on gas content was derived, and coupled to a yield surface considering both inherent and stress-induced anisotropy. The beneficial effect by gas had been considered in the models developed by Pietruszczak and Pande (1996) and Grozic et al. (2005). This is achieved by simplifying the gas bubbles and the pore fluid as a single phase of compressible fluid, which could have beneficially reduced the excess pore water pressure due to undrained shearing, and thus a higher value of s_{u}. Wheeler (1988b) attempted to approximate the damaging and beneficial effects of gas bubbles on the s_{u} value of fine–grained gassy soil, by deriving two separate solutions for the upper and lower bound values for s_{u}. An exact solution for the s_{u} value for a fine–grained gassy soil is still lacking.

Despite the afore–mentioned valuable efforts, the lack of a unified framework to capture both damaging and beneficial effects of gas bubbles on the stress–strain relationship (and thus s_{u} value) of gassy soil has hindered reliable analysis and the design of offshore structures to be built on gassy seabeds. For these reasons, a new elastoplastic constitutive model is proposed in this study to simulate the distinct features of fine–grained gassy soil in a unified manner. The new model was formulated to consider the published experimental evidence associated with the compression behaviour (Thomas 1987; Puzrin et al. 2011; Hong et al. 2017), dilatancy (Hong et al. 2019b) and critical state (Wheeler 1986; Sham 1989; Hong et al. 2017) as well as the new experiments performed in this study that revealed the versatile the shapes of yield surface of the gassy soil. The predictive capability of the model was validated against the results of three types of fine–grained gassy soils, which cover a broad range of u_{w0} and ψ_0.

Key Features of Fine–grained Gassy Soil and Implementations for Constitutive Modeling

The behaviour of fine–grained gassy soil has been investigated during the past three decades through experimental work primarily involving oedometer tests and undrained triaxial compression tests. The key features of the fine–grained gassy soil, including the compression and undrained shear behaviour, are reviewed in this section, with particular emphasis on their implications to the elastoplastic modeling of the soil. It is worth noting that this review and the subsequent theoretical development are concerned mainly with the behaviour of gassy soil under in–situ conditions. The behaviour of fine–grained gassy soil after significant unloading, such as that owing to deep–water sampling which causes bubble expansion and weakening of the soil structure) has been reviewed and modeled by Sultan and Garziglia (2014), and is beyond the scope of this study.

Compression behaviour

Consolidation tests of fine–grained gassy soils based on oedometer (Thomas 1987; Puzrin et al. 2011) and triaxial apparatus (Hong et al. 2017) suggest that gas bubbles and the saturated matrix contribute independently to the total compressibility. This experimental evidence reveals that although gassy soil becomes more compressible at higher gas content, the compressibility of the saturated matrix is not altered by the volumetric gas content. In particularly, the water void ratio e_{w} (i.e., the void ratio of the saturated matrix) is a sole function of the effective mean stress.

These experimental observations have implied three important aspects for the modeling of fine–grained gassy soil (S_{r}>85%): (I) The effective stress principle appears to be valid for describing the behaviour of fine–grained gassy soil; (II) a single set of material constants (e.g., λ and κ as defined in the Modified Cam–clay (MCC) model) can adequately characterize the compression behaviour of the saturated matrix, irrespective of the gas content; and (III) the effective pre–consolidation pressure (p_0') of the soil is not altered by the addition of gas.

Undrained shear strength

A distinct feature of fine–grained gassy soil is that, the presence of gas can either reduce or increase the undrained shear strength s_{u} of the soil at the same consolidation pressure p_0', depending on the initial pore water pressure u_{w0} and ψ_0 (Wheeler 1988b; Hong et al. 2017). Attempts were made to reveal the underlying mechanisms, by analyzing the distributions of the local stress states and local s_{u} values around the bubbles in soils under different values of initial pore water pressure u_{w0} (Wheeler 1988a, 1988b; Sham 1989). The analyses were performed on the basis of rigid–

perfectly plastic cavity contraction analysis on a saturated matrix containing a spherical cavity. It was revealed that the presence of gas bubbles led to two completing mechanisms: (I) shear failure around the bubble, which reduces the global s_{u} of the gassy soil, and (II) heterogeneity of the saturated matrix (i.e., a denser state of soil near the bubble than that in the far field), which increases the global s_{u} of the soil. The former (damaging effect) and the latter mechanisms (beneficial effect) were shown to dominate when the value of u_{w0} was relatively high and low, respectively.

Stress–dilatancy relation

Hong et al. (2019b) experimentally revealed that the addition of gas could make the fine–grained soil either more or less contractive, depending on the combination of u_{w0} and ψ_0. These features cannot be captured by the stress–dilatancy function (D) of the modified Cam–clay model. A new function D was thus developed, by introducing a dilatancy multiplier F that considers the coupling effects of u_{w0} and ψ_0 into the dilatancy function of the MCC model, as follows:

$$\begin{aligned} D = \frac{\mathrm{d}\varepsilon_{\mathrm{v}}^{\mathrm{p}}}{\mathrm{d}\varepsilon_{\mathrm{q}}^{\mathrm{p}}} &= F\left(\frac{u_{\mathrm{w0}} - u_{\mathrm{w0\_ref}}}{p_0'}, \psi_0\right)\frac{M^2-\eta^2}{2\eta} \\ &= \left[1 + \xi\frac{u_{\mathrm{w0}} - u_{\mathrm{w0\_ref}}}{p_0'}\exp\left(-\frac{\chi}{\psi_0}\right)\right]\frac{M^2-\eta^2}{2\eta} \end{aligned} \tag{1}$$

where $F(\frac{u_{\mathrm{w0}} - u_{\mathrm{w0\_ref}}}{p_0'}, \psi_0)$ denotes the dilatancy multiplier; $u_{\mathrm{w0\_ref}}$ denotes the reference u_{w0} at which the stress–dilatancy of a gassy soil is similar to its saturated equivalent. ξ and χ are two material constants for scaling the effects of u_{w0} and ψ_0 on the dilatancy of the gassy soil; and η denotes the stress ratio (i.e., $\eta=q/p'$), where the effective mean stress p' and deviatoric stress q in the triaxial stress space are defined as functions of the major (σ_1') and minor (σ_3') effective principle stresses, as follows:

$$p' = (\sigma_1' + 2\sigma_3')/3 \tag{2}$$

$$q = \sigma_1' - \sigma_3' \tag{3}$$

where M is the stress ratio at the critical state, and p_0' denotes the initial effective mean stress. The proposed function has been validated against the stress–dilatancy relations from 36 tests (series I and II) on gassy specimens and 1 test on a saturated specimen (Hong et al. 2019b). The new function is shown to effectively capture the following key features related to the stress–dilatancy of fine–grained gassy soil:

1. $F\left(\frac{u_{w0}-u_{w0\_ref}}{p_0'}, \psi_0\right) > 1$ when $u_{w0} > u_{w0\_ref}$;and $F\left(\frac{u_{w0}-u_{w0\_ref}}{p_0'}, \psi_0\right) < 1$ when $u_{w0} < u_{w0\_ref}$. This implies that gassy soil at a relatively high initial pore water pressure (when $u_{w0} > u_{w0\_ref}$) exhibits more contractive response than the saturated soil, and vice versa.
2. $F\left(\frac{u_{w0}-u_{w0\_ref}}{p_0'}, \psi_0\right) = 1$ when $u_{w0} = u_{w0\_ref}$, and Eq. (1) is equivalent to the dilatancy relation of the MCC model. This means the two competing mechanisms by the presence of gas, as discussed in the preceding sub–section, are cancelled out for this special case, resulting in gassy soil dilatancy equal to that of its saturated equivalent.
3. $F\left(\frac{u_{w0}-u_{w0\_ref}}{p_0'}, \psi_0\right) = 1$ when $\psi_0 = 0$ (saturated soil), irrespective of the value of u_{w0}. Under this circumstance, Eq. (1) is naturally recovered to the dilatancy relation of the MCC model.
4. $D = 0$ at the critical state ($M = \eta$).

Implied shape of yield curve

It is widely accepted that the shape of the yield curve (on the wet side) of a soil can be reflected by the locus of the undrained effective stress path of a normally consolidated specimen. Hong et al. (2019b) reported undrained effective stress paths of normally consolidated gassy Malaysia kaolin silt, which were prepared at the same value of p_0', 200 kPa, but under different values of u_{w0} at 0, 150, and 600 kPa, as shown in Fig. 2. The loci of these effective stress paths imply that the fine–grained gassy soils exhibit three distinct shapes of yield curves, i.e., teardrop, ellipse and bullet shapes, which occur at relatively low, moderate, and high values of u_{w0}, respectively. Obviously, these variations in the shape of yield curve cannot be captured by the yield function of the MCC model. The results in Fig. 2 suggest the necessity of introducing a versatile function that considers the three distinct shapes of yield curves with a single set of parameters, in the elastoplastic modeling of gassy soil. In addition to the implied shapes of yield curve via effective stress paths (Fig. 2), new experiments are still desired to explicitly reveal the yield curve shapes, and to formulate the relation between the shape and the state of gassy soil. Details are given in the section titled "Experimental Investigation of Yield Curve and Flow Rule."

Critical state

Despite the distinctively different loci of effective stress paths in the $p' - q$ plane for gassy specimens with varying u_{w0} (Fig. 2), their stress ratios at the critical state (i.e., M) are equal to that of the saturated specimen, irrespective of the gas content (Hong et al. 2017). Moreover, the critical state line (CSL) in the $e_{\mathrm{w}} - \ln p'$ plane remains parallel to the normal consolidation line (Wang et al. 2018), with a slope (i.e.,

λ) independent of the gas content. The presence of gas, however, alters the position of the CSL in the $e_{\mathrm{w}} - \ln p'$ plane (Wang et al. 2018) because the gassy soils with the same e_{w} but different values of u_{w0} fail at different p', under undrained shearing.

A New Constitutive Model for Fine–grained Gassy Soils

By considering the key features of fine–grained gassy soil, as reviewed in the preceding section, a new elastoplastic model was developed within the framework of critical state soil mechanics. The model consists of two parts, as shown in Fig. 3: (I) the stress–strain behaviour of the saturated matrix, which is governed by the effective stress principle, and (II) the volume change of gas bubbles owing to gas compression, which is governed by the Boyle's law. The modeling of unsaturated soils requires the proper selection of stress variables (Alonso et al. 1990; Sun et al. 2000; Zhou and Sheng 2015; Zhou and Ng 2016; Gallipoli et al. 2018). It has been justified theoretically (Xu and Xie 2011) and experimentally (Sills et al. 1991; Hong et al. 2017) that the effective stress principle still applies for fine–grained gassy soil with S_{r} exceeding 90%. The usage of effective stress, therefore, has been reported to enable consistent interpretation regarding the analysis of various behaviour of fine–grained gassy soil ($S_{\mathrm{r}} > 90\%$), as revealed by consolidation analysis (Puzrin et al. 2011) and constitutive modeling (Grozic et al. 2005; Sultan and Garziglia 2014) of the soil.

The total volumetric strain of fine–grained gassy soil is a sum of both the volumetric strain of the saturated matrix and gas bubbles (Thomas 1987; Puzrin et al. 2011; Hong et al. 2017). However, the global shear strain of a fine–grained gassy soil is assumed to be identical to that of the saturated matrix because the gas bubbles, with zero shear stiffness, have to deform compatibly with the saturated matrix (Wheeler 1986).

The following sub–sections aim to formulate the stress–strain behaviour of the saturated matrix, except the last sub–section titled "Volumetric behaviour of gas bubbles," which describes the volumetric strain caused by gas compression.

Strain decomposition

Within the elasto–plastic framework, the strain rate tensor ($\mathrm{d}\varepsilon_{ij}$) of the saturated matrix is decomposed into a plastic part ($\mathrm{d}\varepsilon_{ij}^{\mathrm{p}}$) and an elastic part ($\mathrm{d}\varepsilon_{ij}^{\mathrm{e}}$):

$$\mathrm{d}\varepsilon_{ij} = \mathrm{d}\varepsilon_{ij}^{\mathrm{e}} + \mathrm{d}\varepsilon_{ij}^{\mathrm{p}} \tag{4}$$

It is assumed that the saturated soil matrix behaves elastically when its stress state remains within the yield surface, whereas plastic strain is developed once the yield surface is reached. In the triaxial strain space, the work conjugate strain rates for p' and q are the volumetric strain increment ($\mathrm{d}\varepsilon_{\mathrm{v}} = \mathrm{d}\varepsilon_1 + 2\mathrm{d}\varepsilon_3$, where $\mathrm{d}\varepsilon_1$ and $\mathrm{d}\varepsilon_3$ are the major and minor principal strain increments, respectively) and the deviatoric strain increment ($\mathrm{d}\varepsilon_{\mathrm{q}} = 2(\mathrm{d}\varepsilon_1 - \mathrm{d}\varepsilon_3)/3$) of the saturated matrix, respectively. Further, $\mathrm{d}\varepsilon_{\mathrm{v}}$ and $\mathrm{d}\varepsilon_{\mathrm{q}}$ are decomposed into:

$$\mathrm{d}\varepsilon_{\mathrm{v}} = \mathrm{d}\varepsilon_{\mathrm{v}}^{\mathrm{e}} + \mathrm{d}\varepsilon_{\mathrm{v}}^{\mathrm{p}} \tag{5}$$

$$\mathrm{d}\varepsilon_{\mathrm{q}} = \mathrm{d}\varepsilon_{\mathrm{q}}^{\mathrm{e}} + \mathrm{d}\varepsilon_{\mathrm{q}}^{\mathrm{p}} \tag{6}$$

where $\mathrm{d}\varepsilon_{\mathrm{v}}^{\mathrm{e}}$ and $\mathrm{d}\varepsilon_{\mathrm{v}}^{\mathrm{p}}$ denote elastic and plastic volumetric strain increments, respectively, and $\mathrm{d}\varepsilon_{\mathrm{q}}^{\mathrm{e}}$ and $\mathrm{d}\varepsilon_{\mathrm{q}}^{\mathrm{p}}$ are elastic and plastic deviatoric strain increments, respectively. The potential occurrence of bubble flooding, which would impose additional volumetric strain to the saturated matrix by entry of water into the bubble cavity (Wheeler 1988b), has not been considered in this proposed model. It was found experimentally that bubble flooding may rarely occur during undrained shearing (Sham 1989). This was concluded from several undrained triaxial compression tests on gassy Kaolin clayey specimens, which covered a broad range of initial degree of saturation (S_{r0}=92.3% to 99.3%) and initial pore water pressure (u_{w0}=100 to 500 kPa). During the undrained shearing of these gassy specimens, the deduced pore gas pressure (based on the measured gas volume change and Boyle's law) mainly stayed above the measured pore water pressure, suggesting rare occurrence of bubble flooding.

For simplicity, the model is first presented for the triaxial space. More generalized expressions of the model for the multi–axis condition are given in the Appendix.

Elastic behaviour

The elastic behaviour of the saturated matrix is assumed to be isotropic, as routinely exercised in constitutive models for soft clay (Wheeler et al. 2003; Huang et al. 2011; Wang et al. 2012, 2016). The isotropic elastic behaviour is described by the bulk and shear moduli, i.e., K and G, respectively, which are stress–dependent (as a function of p'), as follows:

$$K = \frac{p'}{\kappa/(1+e_{\mathrm{w0}})} \tag{7}$$

$$G = \frac{3(1-2\nu)}{2(1+\nu)}K = \frac{3(1-2\nu)}{2(1+\nu)}\frac{p'}{\kappa/(1+e_{\mathrm{w0}})} \tag{8}$$

where e_{w0} is the initial water void ratio of the gassy soil; κ is the slope of the elastic swelling lines in the $e_{\mathrm{w}}-\ln p'$ plane; ν denotes Poisson's ratio. According to the theory of elasticity, the elastic increments of volumetric and deviatoric strain can be readily calculated using Eqs. (9) and (10), which are the same as those adopted in the

MCC model:

$$\mathrm{d}\varepsilon_{\mathrm{v}}^{\mathrm{e}} = \frac{\mathrm{d}p'}{K} \tag{9}$$

$$\mathrm{d}\varepsilon_{\mathrm{q}}^{\mathrm{e}} = \frac{\mathrm{d}q}{3G} \tag{10}$$

The plastic behaviour of fine–grained gassy soil is formulated in the following sections.

Yield function

To more accurately predict the undrained shear behaviour of fine–grained soil, various forms of functions that predict variable shapes of the yield curve have been proposed by a number of researchers (Lagioia et al. 1996; Yu 1998; Pestana and Whittle 1999; Ling et al. 2002; Yin et al. 2002; Collins 2005; Dafalias et al. 2006; Abuel–Naga et al. 2009; Yin and Chang 2009; Jiang and Ling 2010; Yao et al. 2012; Chen and Yang 2017; Gao et al. 2017). Among them, the yield function Lagioia et al. (1996) is one of the few that are capable of capturing all of the yield surface shapes exhibited by the fine–grained gassy soil (Fig. 2), namely teardrop, ellipse and bullet shapes. Thus, the yield function proposed by Lagioia et al. (1996) was adopted for the elastoplastic modeling of fine–grained gassy soil in this study, as formulated below:

$$f = \frac{p'}{p'_0} - \frac{\left(1 + \frac{\eta}{MK_2}\right)^{\frac{K_2}{(1-\mu)(K_1-K_2)}}}{\left(1 + \frac{\eta}{MK_1}\right)^{\frac{K_1}{(1-\mu)(K_1-K_2)}}} = 0 \tag{11}$$

where p'_0 denotes the pre–consolidation pressure (i.e., the size of the yield surface), and the constants K_1 and K_2 are given by:

$$K_{1/2} = \frac{\mu(1-\alpha)}{2(1-\mu)}\left(1 \pm \sqrt{1 - \frac{4\alpha(1-\mu)}{\mu(1-\alpha)^2}}\right) \tag{12}$$

In the yield function, μ and α are two parameters that enable to flexible adjustment of the shapes of the yield surface. Fig. 4 shows the variations in the yield surface shape with different values of α between 0.03 and 2 but at a constant μ=0.915. As illustrated, the increase in the α value from 0.03 to 2 led to a transition of the yield surface shape on the wet side of the CSL in the following manner: bullet, ellipse, and teardrop shapes. Specifically, this resulted in a yield surface similar to that of the MCC model, when α = 0.4 and μ = 0.915.

One novel contribution in the gassy soil modeling of this study is to investigate and formulate the dependency of the yield surface shape on the key factors governing the yielding of fine–grained gassy soil (e.g., u_{w0} and ψ_0). The functional form of $\alpha\left(\frac{u_{\mathrm{w0}}-u_{\mathrm{w0\_ref}}}{p_0'}, \psi_0\right)$ is proposed considering the experimental observations, as presented in the section titled "Experimental Investigation of Yield Curve and Flow Rule".

Flow rule

As presented, the yield function f (Eq. (11)) and the dilatancy function D (Eq. (1)) were independently formulated in accordance with the experimental evidences. A non–associated flow rule was thus naturally adopted in the proposed gassy soil model (see also Gao et al. 2017):

$$\mathrm{d}\varepsilon_{\mathrm{q}}^{\mathrm{p}} = \langle L\rangle \frac{\partial f}{\partial q} \text{ and } \mathrm{d}\varepsilon_{\mathrm{v}}^{\mathrm{p}} = \langle L\rangle \frac{\partial f}{\partial q} D \tag{13}$$

where L denotes the loading index. The McCauley brackets $<>$ operate in the way of $\langle x\rangle = x$ if $x > 0$; otherwise, $\langle x\rangle = 0$. Direct experimental evidence for the non–associated flow rule is given in the following section. It should be noted that Eq. (13) is an alternative method of defining the non–associated flow rule without explicitly giving the plastic potential function.

Hardening and plastic modulus

Similar to the MCC model, the strain hardening hypothesis is invoked herein, with the plastic volumetric strain increment of the saturated matrix ($\mathrm{d}\varepsilon_{\mathrm{v}}^{\mathrm{p}}$) taken as the sole internal variable for characterizing the evolution of the internal soil structure during the plastic yielding. The following isotropic hardening law (as in MCC) is adopted to relate the expansion or shrinkage of the yield surface size ($\mathrm{d}p_0'$) to the internal variable ($\mathrm{d}\varepsilon_{\mathrm{v}}^{\mathrm{p}}$):

$$\mathrm{d}p_0' = \frac{(1+e_{\mathrm{w0}})}{\lambda-\kappa} p_0' \mathrm{d}\varepsilon_{\mathrm{v}}^{\mathrm{p}} \tag{14}$$

The plastic volumetric strain increment $\mathrm{d}\varepsilon_{\mathrm{v}}^{\mathrm{p}}$ can be calculated by applying the condition of consistency, which ensures that the stress state remains on the yield surface during the plastic yielding, as follows:

$$\mathrm{d}f = \frac{\partial f}{\partial p'}\mathrm{d}p' + \frac{\partial f}{\partial q}\mathrm{d}q + \frac{\partial f}{\partial p_0'}\frac{\partial p_0'}{\partial \varepsilon_{\mathrm{v}}^{\mathrm{p}}}\mathrm{d}\varepsilon_{\mathrm{v}}^{\mathrm{p}} = 0 \tag{15}$$

In Eq. (15), the derivatives $\frac{\partial f}{\partial p'}$, $\frac{\partial f}{\partial q}$ and $\frac{\partial f}{\partial p_0'}$ can be solved on the basis of the yield function (Eq. (11)), and are given below:

$$\frac{\partial f}{\partial p'} = \frac{1}{p_0'} + \frac{\left(1+\frac{\eta}{MK_2}\right)^{\frac{K_2}{(1-\mu)(K_1-K_2)}}}{(1-\mu)(K_1-K_2)\left(1+\frac{\eta}{MK_1}\right)^{\frac{K_1}{(1-\mu)(K_1-K_2)}}} \left(\frac{1}{1+\frac{\eta}{MK_2}} - \frac{1}{1+\frac{\eta}{MK_1}}\right)\frac{q}{Mp'^2} \tag{16a}$$

$$\frac{\partial f}{\partial q} = -\frac{\left(1+\frac{\eta}{MK_2}\right)^{\frac{K_2}{(1-\mu)(K_1-K_2)}}}{(1-\mu)(K_1-K_2)\left(1+\frac{\eta}{MK_1}\right)^{\frac{K_1}{(1-\mu)(K_1-K_2)}}} \left(\frac{1}{1+\frac{\eta}{MK_2}} - \frac{1}{1+\frac{\eta}{MK_1}}\right)\frac{1}{Mp'} \tag{16b}$$

$$\frac{\partial f}{\partial p_0'} = -\frac{p'}{p_0'^2} \tag{16c}$$

According to the theory of plasticity (Dafalias 1986), Eq. (15) can be further expressed as a function of the plastic modulus K_{p} and the loading index L, as follows:

$$\mathrm{d}f = \frac{\partial f}{\partial p'}\mathrm{d}p' + \frac{\partial f}{\partial q}\mathrm{d}q - \langle L\rangle K_{\mathrm{p}} = 0 \tag{18}$$

Combining Eqs. (15) and (18) leads to the following expression of K_{p}:

$$K_{\mathrm{p}} = -\frac{1}{L}\frac{\partial f}{\partial p_0'}\frac{\partial p_0'}{\partial \varepsilon_{\mathrm{v}}^{\mathrm{p}}}\mathrm{d}\varepsilon_{\mathrm{v}}^{\mathrm{p}} \tag{19}$$

Substituting Eqs. (13) and (14) into Eq. (19) yields:

$$\begin{aligned} K_{\mathrm{p}} &= -\frac{(1+e_{\mathrm{w0}})p_0'}{\lambda-\kappa}\frac{\partial f}{\partial p_0'}\frac{\partial f}{\partial q}D \\ &= -\frac{(1+e_{\mathrm{w0}})p_0'}{\lambda-\kappa}\frac{\partial f}{\partial p_0'}\frac{\partial f}{\partial q}\left[1+\xi\frac{u_{\mathrm{w0}}-u_{\mathrm{w0\_ref}}}{p_0'}\exp\left(-\frac{\chi}{\psi_0}\right)\right]\frac{M^2-\eta^2}{2\eta} \end{aligned} \tag{20}$$

With a known K_{p}, the loading index L can be readily calculated by the following equation derived through standard elasto–plasticity procedures:

$$L = \frac{K\frac{\partial f}{\partial p'}\mathrm{d}\varepsilon_{\mathrm{v}} + 3G\frac{\partial f}{\partial q}\mathrm{d}\varepsilon_{\mathrm{q}}}{K_{\mathrm{p}} + K\frac{\partial f}{\partial p'}\frac{\partial f}{\partial q}D + 3G\frac{\partial f}{\partial q}\frac{\partial f}{\partial q}} \tag{21}$$

Elasto–plastic relation of the saturated soil matrix

Having defined the elastic incremental relationship (Eqs. (9) and (10)), and derived the plastic modulus K_{p} (Eq. (19)) as well as the loading index L (Eq. (20)), the elastoplastic relationship can be readily determined. In the triaxial stress space, the incremental stress strain relationship is:

$$\begin{Bmatrix}\mathrm{d}p' \\ \mathrm{d}q\end{Bmatrix} = C_{2\times 2}\begin{Bmatrix}\mathrm{d}\varepsilon_{\mathrm{v}} \\ \mathrm{d}\varepsilon_{\mathrm{q}}\end{Bmatrix} \tag{21}$$

where $C_{2\times 2}$ denotes the elastoplastic matrix, which can be explicitly expressed as:

$$C_{2\times 2} = \begin{bmatrix} K & 0 \\ 0 & 3G\end{bmatrix} - \frac{h(L)}{K_{\mathrm{p}} + K\frac{\partial f}{\partial p'}\frac{\partial f}{\partial q}D + 3G\frac{\partial f}{\partial q}\frac{\partial f}{\partial q}}\begin{bmatrix} K^2\frac{\partial f}{\partial p'}\frac{\partial f}{\partial q}D & 3GK\frac{\partial f}{\partial q}\frac{\partial f}{\partial q}D \\ 3GK\frac{\partial f}{\partial p'}\frac{\partial f}{\partial q} & 9G^2\frac{\partial f}{\partial q}\frac{\partial f}{\partial q}\end{bmatrix} \tag{22}$$

Each term involved in the elastoplastic relation has been derived in the preceding sub–sections. The Heaviside step function $h(L)$ in Eq. (22) works as that $h(L)=1$ if $L>0$, and $h(L)=0$ if otherwise.

The derived constitutive relation (Eqs. (21) and (22)) has enabled the calculation of deviatoric and volumetric strain increments for the saturated matrix with any given stress increments (i.e., $\mathrm{d}p'$ and $\mathrm{d}q$). The former is identical to the global deviatoric strain increment of the fine–grained gassy soil. The latter, in conjunction with the volumetric strain of gas bubbles, as formulated in the following sub–section), form the global volumetric strain of the fine–grained gassy soil.

Volumetric behaviour of gas bubbles

Considering that the typical types of bio–gas (i.e., methane and nitrogen (Lin et al. 2004; Wang et al. 2019)) have extremely low solubility, their volumetric behaviour is predominately induced by gas compression. This can be described using Boyle's law, as follows:

$$(u_{\mathrm{g}}+p_{\mathrm{a}})V_{\mathrm{g}}=(u_{\mathrm{g}}+p_{\mathrm{a}}+\mathrm{d}u_{\mathrm{g}})(V_{\mathrm{g}}+\mathrm{d}V_{\mathrm{g}})=n_{\mathrm{g}}RT=C \tag{23}$$

where u_{g}, p_{a}, V_{g}, n_{g}, R, and T denote the pore gas pressure, atmospheric pressure, gas volume, number of the mole of the gas, ideal gas constant and absolute temperature, respectively; and $\mathrm{d}u_{\mathrm{g}}$ and $\mathrm{d}V_{\mathrm{g}}$ are increment of gas pressure and gas volume, respectively; The constant C can be calculated by the initial pore gas pressure u_{g0} and the initial gas volume V_{g0} as

$$(u_{\mathrm{g0}}+p_{\mathrm{a}})V_{\mathrm{g0}}=C \tag{24}$$

According to Sham (1989), the initial gas pressure u_{g0} falls between the initial pore water pressure u_{w0} and initial total stress p_0, leading to the equation below:

$$u_{\mathrm{g0}} = u_{\mathrm{w0}} + \delta(p_0 - u_{\mathrm{w0}}) \tag{25}$$

where δ is a parameter ranging from 0 to 1. The increment of the gas pressure $\mathrm{d}u_{\mathrm{g}}$ was assumed to vary equally as the increment of the total stress $\mathrm{d}p$. This permits a higher increasing rate of pore water pressure than that of gas pressure for a normally or slightly over–consolidated soil (contractive material) subjected to undrained shearing, i.e., $\mathrm{d}u_{\mathrm{w}} > \mathrm{d}p = \mathrm{d}u_{\mathrm{g}}$. Under this circumstance, the proposed model should have predicted the value of u_{w} to approach u_{g} during the undrained shearing. Once the difference between u_{g} and u_{w} has stayed below a water entry value (i.e., $2T/r$, where T and d are surface tension for a water–air interface and bubble cavity radius, respectively), the gas pressure is insufficient to resist water entry into the bubble cavity from the saturated matrix due to the flat surface of the menisci at the water–bubble interface, causing bubble flooding (Wheeler 1988b; Wheeler et al. 1990). In other words, the proposed model may phenomenologically capture the trend that will cause initiation of bubble flooding. The calculated evolution of $u_{\mathrm{g}} - u_{\mathrm{w}}$ values in typical undrained shear tests, which suggest the likelihood of bubble flooding, are given and discussed in the following sub–section 'Shear behaviour'. The term $\mathrm{d}V_{\mathrm{g}}$ can be then deduced by combining Eqs. (23), (24) and (25) as

$$\begin{aligned} \mathrm{d}V_{\mathrm{g}} &= -\frac{\mathrm{d}u_{\mathrm{g}} V_{\mathrm{g}}}{u_{\mathrm{g}} + p_{\mathrm{a}} + \mathrm{d}u_{\mathrm{g}}} = -\frac{\mathrm{d}u_{\mathrm{g}}\left(u_{\mathrm{g0}} + p_{\mathrm{a}}\right)V_{\mathrm{g0}}}{\left(u_{\mathrm{g}} + p_{\mathrm{a}} + \mathrm{d}u_{\mathrm{g}}\right)\left(u_{\mathrm{g}} + p_{\mathrm{a}}\right)} \\ &= -\frac{\mathrm{d}p(u_{\mathrm{w0}} + p_{\mathrm{a}})(2p_0 + p_{\mathrm{a}} - u_{\mathrm{w0}})V_{\mathrm{g0}}}{\left(u_{\mathrm{g}} + p_{\mathrm{a}} + \mathrm{d}p\right)\left(u_{\mathrm{g}} + p_{\mathrm{a}}\right)(p_0 + p_{\mathrm{a}})} \end{aligned} \tag{26}$$

The volumetric strain increment of gas owing to bubble compression can thus be obtained, as follows:

$$\mathrm{d}\varepsilon_{\mathrm{v}}^{\mathrm{g}} = \frac{\mathrm{d}V_{\mathrm{g}}}{V} = -\frac{\mathrm{d}p(u_{\mathrm{w0}} + p_{\mathrm{a}})(2p_0 + p_{\mathrm{a}} - u_{\mathrm{w0}})\psi_0}{(u_{\mathrm{g}} + p_{\mathrm{a}} + \mathrm{d}p)(u_{\mathrm{g}} + p_{\mathrm{a}})(p_0 + p_{\mathrm{a}})} \tag{27}$$

The above formulations were derived following the routine practice (Thomas 1987; Wheeler 1988a; Wheeler et al. 1990) for estimating gas pressure and volumetric behaviour of gas bubbles using Boyle's law. In this simplified approach, the effect of changing surface tension (by the small menisci forming at the interface between the gas bubbles and pore water) on gas pressure variation has not been explicitly considered. This could have led to some errors in predicting the volumetric behaviour of gas bubbles, as detailed in the section "Compression behaviour". On the other hand, the capability of the proposed model for predicting the shear behaviour of the saturated matrix, which is a primary focus of this study, is merely affected by the simplification using Boyle's law. Because the only gas–related variable governing the shear behaviour is the initial gas volume fraction, which is measurable experimentally.

It is worth noting that the model proposed herein was derived by assuming that the discrete bubbles form stably within the soil, which consistently impose a certain degree of detrimental or beneficial effect in the soil. This assumption has been justified experimentally by Hong et al. (2017). In their triaxial test, a constant isotropic cell pressure of 320 kPa and back pressure of 120 kPa were imposed to a gassy specimen for 24 h, which is twice of the duration required for a typical undrained triaxial compression test for fine–grained gassy soil. The total volume of the gassy specimen under the constant load was almost identical, which suggests that the nitrogen bubbles were stably formed and their modification effect on the soil did not vanish with time.

Experimental Investigation of Yield Curve and Flow Rule

A series of undrained triaxial tests was conducted on reconstituted gassy Malaysia kaolin. The primary objectives of the experimental investigation were (I) to verify the modeling concepts incorporated in the new model, particularly the hypothesized shapes of yield curve and non–associated flow rule, and (II) to formulate the dependency of the yield surface shape on the key factors governing the yielding of fine–grained gassy soil, i.e., a functional form $\alpha\left(\frac{u_{\mathrm{w0}}-u_{\mathrm{w0\_ref}}}{p_0'}, \psi_0\right)$ related to the yield curve shape. Several preliminary test results are reported in Hong et al. (2019b).

Experimental program and setup

The program consists of two series of strain–controlled undrained triaxial compression tests. The test series I and II aimed to address the afore mentioned objectives (I) and (II), respectively. The program of test series II and part of the experimental data had been reported in Hong et al. (2019b).

In test series I, a total of 24 tests were performed on OC specimens under an isotropic stress condition. As summarized in Table1, the program was divided into four groups including Groups A, B and C for gassy specimens containing the same amount of gas, 4.6 x10^{-4} mole, at different values of u_{w0} at 0, 150, and 600 kPa, and Group D for saturated specimens. Each group consisted six specimens, having the same size of yield surface, $p_0' = 200\mathrm{kPa}$ but with different current effective mean stresses, at p_{i}'=120, 140, 160, 170 180, and 190 kPa. The undrained shear tests of the six OC specimens in each group led to the identification of six yield points that defined the shape of the yield curve and the directions of the plastic strain increments at the six points.

Test series II included 18 tests on gassy specimens and 1 reference test on a saturated specimen, as summarized in Table 2. The experimental program considered a wide range of initial pore water pressures, at $u_{\mathrm{w0}} = 0 - 600\mathrm{kPa}$, and initial gas volume fractions, at $\psi_0 = 0.6 - 6.3\%$, aiming to offer representative experimental results for formulating the shape–related functional form $\alpha\left(\frac{u_{\mathrm{w0}} - u_{\mathrm{w0\_ref}}}{p_0'}, \psi_0\right)$.

The experimental investigation was performed using a GDS triaxial apparatus equipped with a HKUST double–cell (Ng et al. 2002) for measuring changes in the degree of saturation (S_r) and gas volume fraction (ψ) during the test of each gassy specimen. All of the tests were performed in a lab with controlled room temperature at T=25°± 2°. The double cell system was calibrated to account for the apparent volume change caused by the deformation of the inner cell and drainage lines owing to variation in cell pressure, temperature and creep, and by the movement of the loading ramp relative to the inner cell (Ng et al. 2002). The estimated accuracy of the double–cell system was equivalent to a volumetric strain of 0.05 % for each gassy specimen.

Testing material and preparation of gassy specimen

Given the difficulty in obtaining intact gassy samples from the field owing to gas expansion upon unloading, reconstituted gassy specimens were replicated in this experimental investigation, as routinely exercised in relevant studies (Wheeler 1988b; Sham 1989; Lunne et al. 2001; Sultan et al. 2012).The gassy specimens were prepared by introducing nitrogen, a typical bio–gas, into saturated Malaysia kaolin using the zeolite molecular sieve technique (Nageswaran 1983). Table 3 shows the index properties of the kaolin. This technique been used to yield repeatable gassy specimens with controllable gas contents (Wheeler 1988b; Sham 1989; Hong et al. 2017). Details of this technique are given in Nageswaran (1983).

The replicated gassy soils were carefully trimmed to form standard triaxial specimens with a diameter and height of 50 mm by 100 mm, respectively. They were then transferred to the triaxial cell for isotropic consolidation under the same p'_0 (i.e., 200 kPa) but different u_{w0} values (i.e., 0, 50, 150, 300 and600 kPa).

Experimental procedure

Each test in series I, as listed in Table 1, were performed according to the following procedures:

1. impose a drained isotropic unloading path to each normally consolidated gassy specimen, to bring its stress state to different points within the yield surface such as 120, 140, 160, 170, 180, and 190 kPa;
2. applying undrained triaxial compression to each specimen at a constant axial strain rate of 1.5%/h until reaching the critical state;
3. forcibly saturate each specimen by increasing the cell pressure (under the undrained condition) until no further development of volume change is noted. This procedure is used to obtain the final gas volume after reaching the critical state, and thus to back–calculate the values of S_r and ψ during the entire process of each test (Wheeler 1988b; Sham 1989; Hong et al. 2017).

The tests in series II (Table 2) were performed following procedures (2) and (3), as listed above.

Distinct shapes of yield curve

The shape of each yield curve was determined by extrapolating the yield points identified from the results of test series I. A yield point is defined by the effective means stress and deviatoric stress at the onset of yielding, i.e., p'_{y} and q_{y}. Following Cekerevac and Laloui (2004), the yield stresses were deduced by applying the bilinear plotting techniques (Graham et al. 1982) to two independent sets of data in each test, namely $q-\varepsilon_{\mathrm{q}}$ and $W-\eta$ relations, where W is the total strain energy). Typical examples of deducing yield points are shown in Fig. 5, whereas the yield stresses for all tests are summarized in Table 4. In each test, the yield stresses deduced from the two criteria are broadly consistent, with a percentage difference smaller than 14%. Thus, the average results from the two criteria were taken as the yield stresses at each yield point.

Fig. 6 shows four groups of yield points (from Groups A, B, C and D in test series I, Table 1) in the $q-p'$ plane normalized by their preconsolidation pressure ($p'_0 =$ 200kPa). Each group of yield points was best–fitted with the yield function adopted in this study (Eq. (11)), where the parameter M is 1.05 (Hong et al. 2019b). The shape parameter μ of the yield function was fixed at 0.915, whereas the other shape parameter α was fine–tuned to fit each group of yield points.

The figure reveals that for the saturated specimen, the yield curve on the wet side of the critical state exhibited an ellipse shape, as anticipated. The addition of a small fraction of gas bubbles into the soil significantly altered the shape of the yield curve in different manners, depending on the value of u_{w0}. Three distinctive shapes of yield curve including bullet, ellipse, and teardrop shapes were noted on the wet side when relatively high, intermediate, and very low values of u_{w0} at 600 kPa, 150 kPa, and 0 kPa were imposed, respectively.

Although the yield function (i.e., Eq. (11)) is defined based on stresses within the matrix, it is still likely to be valid for describing the overall yield behaviour of soils containing a small fraction of gas, where the effective stress principle approximately works for the entire gassy soil. Xu and Xie (2011) derived the effective stress for fine–grained soil containing discrete bubbles based on three–phase equilibrium analysis of a representative element volume (REV), as a function of total stress, pore water pressure, pore gas pressure and surface tension. Using their equation, it can be readily calculated that for all the gassy specimens summarized in Table 1 (for studying yield loci), the initial effective mean stress p' in saturated matrix of each specimen only deviates from the corresponding 'overall' p' of the entire gassy specimen by 1% (i.e., 1.2 kPa for specimen G0_120). Meanwhile, the 'overall' deviatoric stress imposed to each gassy specimen is anticipated to be the same as that taken locally by the saturated matrix, because the gas bubbles cannot sustain shear stress. It is therefore a reasonable approximation to use the yield function based on stresses defined for the saturated matrix (Eq. (11)) to describe the overall yield behaviour of soils containing a small fraction of gas.

The observed shapes of the yield loci have revealed the underlying mechanisms of the gas bubble effect in the context of elasto–plastic modeling. The presence of gas bubbles at a relatively high u_{w0} value (600 kPa) led to shrinkage of the area of elastic domain, as compared with that of the saturated specimen. This is likely associated with the localized shear failure induced initially in the saturated matrix surrounding the bubbles, which plays a dominant role at high u_{w0} (Wheeler 1988b; Sham 1989). Conversely, the presence of gas bubbles at a low u_{w0} (0 kPa) resulted in an expanded area of elastic domain relative to that of the saturated specimen. This is likely attributed to the dominant effect of localized matrix heterogeneity at low u_{w0}, which causes the saturated matrix around the gas bubbles to be lightly OC, thus expanding the yield surface (Sham 1989). The area of the elastic domain at a moderate u_{w0} of 150 kPa was quite similar to that of the saturated specimen, which suggests that the effects of the aforementioned competing mechanisms are likely cancelled out under this circumstance. This experimental evidence verifies the concept of adopting a versatile expression of the yield function (Eq. (11)) in the proposed model, which can reproduce the three distinct shapes of the yield curve by varying the shape parameter α. To enable unified modeling of the variable yield curves of the gassy soil with a single set of parameters, the term α should be formulated as a functional form that adequately captures the combined effects of u_{w0} and ψ_0. The functional form is proposed subsequently, based on the results of test series II.

Direction of plastic strain increment and flow rule

Fig. 6 also shows the incremental plastic strain vector (i.e., resultant vector of $\mathrm{d}\varepsilon_{\mathrm{v}}^{\mathrm{p}}$ and $\mathrm{d}\varepsilon_{\mathrm{q}}^{\mathrm{p}}$) at each yield point. The increments of plastic volumetric and deviatoric strain, which determines the direction of the incremental plastic strain vector, were calculated using Eqs. (5), (6), (9) and (10). In the calculation, the stress increment was taken as 20kPa, which is 1/10 of the pre–consolidation pressure p_0' (Cekerevac and Laloui

2004).

As illustrated, the direction of the plastic strain vectors of the saturated specimen (Group D) and the gassy specimen at an intermediate $u_{w0} = 150$kPa (Group B) aligned roughly perpendicular to their yield curves. The "deviation" of the plastic strain increment vectors varied between –5° and 2°, as summarized in Table 5. However, these are significant deviations between the direction of the plastic strain vectors and the normality of the yield curves, for the gassy specimens in Groups A and C with a low and a relatively high u_{w0} of 0 and 600 kPa, respectively. The deviation angles were in the range of –68° to 37° (Table 5). This verifies the concept of adopting a non–associated flow rule (Eq. (13)) in the proposed model.

The dependency of plastic flow direction (i.e., dilatancy) of fine–grained gassy soil on u_{w0} and ψ_0 was incorporated into the dilatancy function (as published in Hong et al. 2019b). This was achieved by introducing a dilatancy multiplier $F\left(\frac{u_{w0}-u_{w0\_ref}}{p_0'}, \psi_0\right)$ to scale the dilatancy function of the MCC model, as shown in Eq. (1). Fig. 7 compares the measured and the predicted dilatancy multiplier $F\left(\frac{u_{w0}-u_{w0\_ref}}{p_0'}, \psi_0\right)$ deduced from results of test series I and II, which validate the dilatancy function (Eq. (1)) used in the proposed model.

Formulating functional forms for $\alpha\left(\frac{u_{w0}-u_{w0\_ref}}{p_0'}, \psi_0\right)$

Based on the results of test series I and II covering a broad range of u_{w0} and ψ_0, the dependency of the yield shape related functional forms $\alpha\left(\frac{u_{w0}-u_{w0\_ref}}{p_0'}, \psi_0\right)$ on the two variables can be formulated. Because the locus of the undrained effective stress reflects the shape of yield curve (as shown in Figs. 2 and 6), the proposed model was calibrated against the stress paths from the tests to obtain the α value of each specimen. All back–calculated α values were then plotted against ψ_0 and $\frac{u_{\mathrm{w0}}-u_{\mathrm{w0\_ref}}}{p_0'}$ of the corresponding specimen, as shown in Fig. 8.

Inspection of the trends in Fig. 8 suggests that the $\alpha\left(\frac{u_{\mathrm{w0}}-u_{\mathrm{w0\_ref}}}{p_0'}, \psi_0\right)$ value exceeds 0.4 when $u_{\mathrm{w0}} < u_{\mathrm{w0\_ref}}$ and increases exponentially with ψ_0 for each given $\frac{u_{\mathrm{w0}}-u_{\mathrm{w0\_ref}}}{p_0'}$. However, $\alpha\left(\frac{u_{\mathrm{w0}}-u_{\mathrm{w0\_ref}}}{p_0'}, \psi_0\right)$ value fell within the range of 0 to 0.4 when $u_{\mathrm{w0}} > u_{\mathrm{w0\_ref}}$, with its value decaying exponentially with ψ_0 for each given $\frac{u_{\mathrm{w0}}-u_{\mathrm{w0\_ref}}}{p_0'}$. When $u_{\mathrm{w0}} = u_{\mathrm{w0\_ref}}$, $\alpha\left(\frac{u_{\mathrm{w0}}-u_{\mathrm{w0\_ref}}}{p_0'}, \psi_0\right)$ was nearly a constant value of 0.4, irrespective of the gas volume fraction ψ_0 (including the saturated case, where $\psi_0 = 0$). This experimental evidence led to the formulation of $\alpha\left(\frac{u_{\mathrm{w0}}-u_{\mathrm{w0\_ref}}}{p_0'}, \psi_0\right)$ as follows:

$$\alpha\left(\frac{u_{\mathrm{w0}}-u_{\mathrm{w0\_ref}}}{p_0'}, \psi_0\right) = 0.4 * \exp\left(-5 * \Lambda \psi_0^{a+h(\Lambda)b}\right) \tag{28}$$

In the equation, $\Lambda = \frac{u_{\mathrm{w0}}-u_{\mathrm{w0\_ref}}}{p_0'}$, which measures the normalized difference of the initial water pressure u_{w0} from a virtual reference initial water pressure $u_{\mathrm{w0\_ref}}$. The presence of gas would beneficially expand the area of elastic domain when $\Lambda < 0$, but would detrimentally shrink it when $\Lambda > 0$. The two soil constants a and b control the relative effectiveness of Λ and ψ_0 in determining the shape of the yield curve. It is worth noting that the sensitivity of ψ_0 to α is altered when the sign of Λ changes. Therefore, a Heaviside step function $h(\Lambda)$ was incorporated in the power of ψ_0 to capture the different effects, i.e., the power of ψ_0 is $(a + b)$ and a, when $\Lambda > 0$ (damaging effect) and $\Lambda < 0$ (beneficial effect), respectively. The factor "5" in Eq. (28)

is a default value independent of the initial conditions (including ψ_0 and u_{w0}) and the soil type, as evident from the three types of fine–grained gassy soils simulated in this study (Table 6).

The proposed form of $\alpha\left(\frac{u_{\mathrm{w0}}-u_{\mathrm{w0\_ref}}}{p'_0}, \psi_0\right)$ can capture the following key features of fine–grained gassy soils:

1. When $u_{\mathrm{w0}} > u_{\mathrm{w0\_ref}}$, the shape–related term α is smaller than 0.4, causing a bullet shape in the yield curve. This simulates the detrimental role of gas in shrinking the area of elastic domain.
2. When $u_{\mathrm{w0}} < u_{\mathrm{w0\_ref}}$, the shape–related term α exceeds 0.4, causing a teardrop shape in the yield curve. This models the beneficial role of gas in expanding the area of elastic domain.
3. When $u_{\mathrm{w0}} = u_{\mathrm{w0\_ref}}$, the shape–related term α becomes 0.4. For this special case, the shape of the yield curve is very close to an ellipse, and the gassy soil behaves similarly to its saturated equivalent.
4. Upon reaching saturation (ψ_0=0), α is equal to 0.4, irrespective of the u_{w0} values. The shape of the yield curve becomes very similar to that of the MCC, and the proposed model is recovered to a conventional critical state model for saturated fine–grained soil.

Determination of Model Parameters

Standard experimental procedure for parameter determination

The new model includes ten parameters. In addition to the five conventional parameters of λ, κ, N, v, and M from the MCC model, two new parameters controlling the shape of the yield curve (a and b) and two new parameters governing the stress–dilatancy (ξ and χ) and one new parameter relating to the initial gas pressure (δ) are introduced in the new model. The parameter δ is not compulsory, if the prediction for the volumetric behaviour of the gassy soil were not intended. These parameters can be conveniently determined from the results of conventional oedometer and triaxial tests in the following ways:

1. The MCC model parameters λ, κ, N, v, and M can be obtained following well–established procedures such as those recommended by Wood (1990), based on conventional oedometer and triaxial tests conducted on saturated specimens;
2. ξ and χ controlling the stress–dilatancy can be fine–tuned to fit the dilatancy function (Eq. (1)) against the measured stress – dilatancy relations of fine – grained gassy soil. Hong et al. (2019b) performed the calibration against the results of four undrained triaxial tests, which were undertaken at two values of u_{w0} with one each exceeding and remaining below $u_{\mathrm{w0\_ref}}$, with two different values of ψ_0 at each u_{w0}.
3. a and b controlling the shape of the yield curve can be determined by calibrating the undrained effective stress paths of the same triaxial tests mentioned in item (2) on the basis of the seven pre–determined parameters (i.e., λ, κ, N, v, M, ξ, and χ).
4. δ can be tuned by fitting the compression curves of gassy specimen (under either 1D or isotropic conditions).

These procedures were used to determine the model parameters of three types of fine–grained gassy soils published in the literature, as summarized in Table 6. The test results of these fine–grained gassy soils were used for verifying the new model proposed in this study, as presented in the following section.

Correlation of the four new model parameters to Atterberg limits

As shown in Table 6, the values of the new parameters (a, b, ξ and χ) appeared to vary significantly among the three gassy soils. An attempt was therefore made to explore whether the new parameters followed a particular certain trend, by examining their correlations to the intrinsic soil properties (e.g., Atterberg limits). It was encouraging to find that each new model parameter exhibited an approximate linear correlation to the plastic index (I_{p}) of the soils (see Fig. 9), with the coefficient of determination (R^2) for each parameter being no smaller than 0.87. These correlations may offer an alternative way for estimating the four new model parameters, given the lack of experimental results.

Model Validation

To adequately verify the new gassy soil model, all published experimental results, to the authors' best knowledge, on the behaviour of fine–grained gassy soil under in–situ stress conditions without experiencing unloading were collected. These include tests on three types of gassy fine–grained soils, i.e., gassy Combwich mud (Wheeler 1986; Thomas 1987), gassy Kaolin clay (Sham 1989) and gassy Malaysia kaolin (Hong et al. 2019), which cover a wide range of initial pore water pressure of 0–600kPa and degree of saturation S_{r} at 88.2–100%. On the basis of their Atterberg limits, compared with the values of the British Standards Institution (BSI, 1999), the Combwich mud, Kaolin clay and Malaysia kaolin were characterized as silt with very high plasticity, clay with high plasticity and silt with high plasticity, respectively. This suggests that the test results adopted for validation are representative of those exhibited by most fine–grained gassy soil.

The gassy soil specimens in the above experiments (including compression and triaxial shear tests) for model validation were all prepared using the zeolite molecular sieve technique, which closely mimic the process of bubble formation within fine–grained marine sediments (Sills et al. 1991). This is could have led to similar micro–structure of the three gassy soils, which could be simulated by the proposed model in a consistent manner.

Compression behaviour

Figs. 10(a) and 10(b) show comparisons between the measured and predicted compression behaviour of one–dimensionally consolidated Combwich mud (Thomas 1987) and isotopically consolidated Malaysia kaolin, respectively, with different ψ_0. The gassy Combwich mud specimens were charged with various amounts of methane at ψ_0=2.1% and 12.7% and were consolidated under u_{w0}=0 kPa. The gassy Malaysia kaolin specimens were charged with the same amount of nitrogen, which exhibited different ψ_0 between 0.7% and 9.2% owing to the varying values of u_{w0} imposed, at 0–1000kPa. It can be seen from Figs. 10(a) and (b) that the proposed model can broadly capture the compression behaviour of gassy and saturated specimen of the two soils, with a maximum percentage difference of 17%. To improve the model prediction, the effect of changing surface tension (by the small menisci forming at the water–gas bubble interface) on gas pressure variation should be explicitly considered in future, because the gas pressure affects the compression of the gas bubbles in this model.

While calculating the above compression curves with the proposed model, it was found that the parameter δ (controlling the initial gas pressure, see Eq. (25)) is a material constant independent of the initial gas content and pore water pressure, i.e., δ = 0.6 and 0.7 for Combwich mud and Malaysia kaolin, respectively. This suggests the validity of Sham (1989)'s equation as a first approximation for the initial gas pressure.

Shear behaviour

Fig. 11 compares the measured and predicted undrained shear behaviour (i.e., stress–strain relation, excess pore water pressure and effective stress path) of typical gassy Malaysia kaolin specimens having a wide range of initial pore water pressure, at u_{w0}=0–600 kPa) and gas volume fractions, at ψ_0=0.6%–6.3%). As illustrated in the figure, the proposed model is capable of reasonably reproducing the various shear behaviour measured in the experiments. In particular, the proposed model managed to capture the directions of the initial portions of the effective stress paths owing to a very small $\mathrm{d}\eta$ of η=0, i.e., an initially inclining stress path ($\mathrm{d}p' < 0$) for the gassy specimen with $u_{\mathrm{w0}} = 600$kPa, and a stress path with delayed inclining compared with that of saturated specimen for the gassy specimen with $u_{\mathrm{w0}} = 0$kPa. The former is associated with an inelastic response during the very early stage of shearing (Yang et al. 2016), whereas the latter implies a delayed onset of yielding compared with that of its saturated equivalent). These features were reproduced by introducing the physically robust yield function f and the dilation function D in the proposed model, which reasonably predicted the plastic volumetric strain ($\mathrm{d}\varepsilon_\mathrm{v}^\mathrm{p} = \langle L \rangle \frac{\partial f}{\partial q} D$) and elastic volumetric strain ($\mathrm{d}\varepsilon_\mathrm{e}^\mathrm{p}$=$-\mathrm{d}\varepsilon_\mathrm{v}^\mathrm{p}$ under the undrained condition), and thus $\mathrm{d}p'$ at very small η.

Figs. 12 and 13 show comparisons between the measured and predicted undrained shear responses of gassy Combwich mud (Wheeler 1986) and gassy Kaolin clay (Sham 1989), respectively. Because only one set of data on the full curves of undrained shear responses was reported for each soil (Figs. 11 and 12), it is not possible to rigorously calibrate all parameters following the standard procedures suggested in the preceding section. Trial–and–errors were employed to best–tune the model parameters, based on the single set of data on the undrained shear responses, and the large numbers of measured undrained shear strength for each soil. The model parameters of gassy Combwich mud and gassy Kaolin clay are summarized in Table 6， while the calibrated reference initial water pressure $u_\mathrm{w0\_ref}$ of the former and the latter are 20 kPa and 50 kPa, respectively. Given the lack of rigor in the calibration, the model predictions for the two soils still show broadly agreements with the experimental results.

Undrained shear strength

Figs. 14, 15 and 16 show the comparisons between the measured and predicted undrained shear strength (s_u) of gassy Malaysia kaolin silt, Combwich mud, and Kaolin clay at various combinations of u_w0 and ψ_0, respectively. In each figure, the strength of the gassy specimens ($s_\mathrm{u\_gas}$) was normalized by that of the saturated specimen ($s_\mathrm{u\_sat}$) having the same p_0'. When the $s_\mathrm{u\_gas}/s_\mathrm{u\_sat}$ ratio was lower than the unity, the gas bubbles posed a damaging effect to the soil, and vice versa. As shown in the figures, the proposed model is able to capture both the damaging and beneficial effects of gas on s_{u} of the gassy soils for each soil, with a unified set of model parameters. Quantitatively, the percentage difference between the measured and predicted values of s_{u} for gassy Malaysia Kaolin silt, in which all model parameters were determined via rigorous calibrations, was no larger than 10%. Higher percentage differences of 15% and 16%were obtained when predicting s_{u} for gassy Combwich mud and Kaolin clay, respectively, owing to the lack of experimental results for rigorously calibrating their model parameters, such as effective stress paths and stress–dilatancy relations at different u_{w0} values.

Quantifying the 'detrimental' and 'beneficial' effect of gas: a parametric study

Based on the validated model and model parameters of the three fine–gained gassy soils, as presented above, a program of parametric study was performed to quantify the modification effect of gas on the s_{u} values of the gassy soils. For each soil, 10000 sets of combinations that cover a broad range of initial pore water pressure (u_{w0}= 0–1000 kPa) and initial gas volume fraction (ψ_0= 0–10%) at a given initial effective stress (p'_0=200 kPa) were considered in the parametric study.

Fig. 17(a), 17(b) and 17(b) show the calculated results of gassy Malaysia kaolin silt (I_{p}=27), gassy Combiwich mud (I_{p}=28) and gassy Kaolin clay (I_{p}=32), respectively. In each figure, the undrained shear strength of gassy soil is normalized by that of its saturated equivalent, i.e., $s_{\mathrm{u\_gas}}/s_{\mathrm{u\_sat}}$, for identifying 'detrimental' or 'beneficial' effect by presence of gas. It can be seen that the modification effect of gas on the undrained shear strength of fine–grained soil greatly varies. Presence of gas can either reduce undrained shear strength by 25%, or increase it by 40%, depending on the coupling effect between ψ_0 and u_{w0} (as featured by the dimensionless variable Λ). For each soil with a given Λ, the change of soil strength by presence of gas (either 'detrimental' or 'beneficial') increases with initial gas volume fraction ψ_0, but at a decreasing rate. The calculation charts, as shown in Fig. 17, may assist with the preliminary design of offshore structures founded on a gas–bearing fine–grained sediments with relevant plastic indexes (I_p).

Conclusions

This study presents a new elastoplastic critical state constitutive model for fine–grained gassy soil. The model was formulated for the triaxial and generalized three–dimensional (3D) stress conditions as described in the Appendix).

Unlike existing models which solely consider either detrimental or beneficial effect of gas on fine–grained soil, the new model captures both the damaging and beneficial effects of gas bubbles on the stress–strain behaviour of gassy soils in a unified manner. This was achieved by incorporating a versatile expression of yield function and a dilatancy function of gassy soils, which account for the coupling effects of ψ_0 and u_{w0}, into the elastoplastic framework in conjunction with the concept of critical state.

Compared with the MCC model, four additional model parameters are introduced in the proposed model, for describing the effects of gas on the yield surface shape and stress–dilatancy of fine–grained gassy soil. All parameters can be determined through routine oedometer and triaxial tests. The four new model parameters almost linearly correlated with the plastic index (I_p) of the soil, offering an alternative way to approximate these parameters.

The proposed model reasonably predicted the behaviour of three different types of fine–grained gassy soils covering a wide range of ψ_0 and u_{w0}, with a single set of parameters. The distinct features of the fine–grained gassy soil, which had been treated separately or partly in the existing models, can now be captured by the new model within a unified framework. The model's benefits are summarized in the following points.

1. The versatile expression of yield function can model, in a unified context, the distinct shapes of yield curve such as bullet, ellipse, and teardrop shapes) for fine–grained gassy soils over a wide range of ψ_0 and u_{w0}. This has enabled the model to consider the role of gas in either contracting or expanding the area of the elastic domain at a given pre–consolidation pressure p'_0.
2. By suitable adjustment of the elastic domain area, the model can reproduce an inelastic response during the very early stage of shearing (under a small $\mathrm{d}\eta$ at $\eta = 0$) of fine–grained gassy soil at a high u_{w0} or a delayed onset of yielding than that of its saturated equivalent) for gassy soil with a low u_{w0}. This explains the different initial directions of their undrained effective stress paths, i.e., an initially inclined stress path ($\mathrm{d}p' < 0$) owing to an inelastic response and delayed inclination the stress path when the elastic domain expands.
3. The adopted dilatancy function (as published in Hong et al. (2019b)) can model the role of gas in either suppressing or enhancing the dilatancy of the gassy soil compared with the ability of their saturated equivalents over a broad range of ψ_0

and u_{w0} with one set of parameters.

4. By coupling the dilatancy function to the versatile yield surface, the model can predict a reduction or increase in the undrained shear strength (s_{u}) owing to the presence of gas. The former (damaging) effect is achieved by shrinking the yield curve to a bullet shape while enhancing the contraction. This leads to an increased positive excess pore water pressure and therefore a lower s_{u} than those of the saturated equivalent. The latter (beneficial) effect can be reproduced in the opposite manner.

One missing feature of fine–grained gassy soil in the proposed model is related to the unloading stress path, which will cause plastic damage to the soil structure (Sultan et al. 2012). The current model does not capture this feature because it predicts only the elastic response in unloading. Future improvements will be made by introducing the bounding surface plasticity (Dafalias 1986) into the current model to consider the plastic strain upon unloading.

Appendix. Generalization of the Model for Multiaxial Stress Space

Definitions

The stress and strain tensors used in the generalization are defined as follows:

deviatoric stress

$$s_{\mathrm{ij}} = \sigma'_{\mathrm{ij}} - p'\delta_{\mathrm{ij}} \tag{29}$$

mean effective stress

$$p' = \frac{1}{3}\sigma'_{\mathrm{ij}}\delta_{\mathrm{ij}} = \frac{1}{3}\sigma'_{\mathrm{ii}} = \frac{1}{3}(\sigma'_{11} + \sigma'_{22} + \sigma'_{33}) \tag{30}$$

The scalar value of deviatoric stress q, used in the simplified version of the model for triaxial space, is the defined by:

$$q = \sqrt{\frac{3}{2}s_{\mathrm{ij}}s_{\mathrm{ij}}} \tag{31}$$

deviatoric strain increment

$$\mathrm{d}e_{\mathrm{ij}} = \mathrm{d}\varepsilon_{\mathrm{ij}} - \frac{1}{3}\mathrm{d}\varepsilon_{\mathrm{v}}\delta_{\mathrm{ij}} \tag{32}$$

volumetric strain increment

$$\mathrm{d}\varepsilon_{\mathrm{v}} = \mathrm{d}\varepsilon_{\mathrm{ii}} = \mathrm{d}\varepsilon_{11} + \mathrm{d}\varepsilon_{22} + \mathrm{d}\varepsilon_{33} \tag{33}$$

The scalar value of deviatoric strain increment $\mathrm{d}\varepsilon_{\mathrm{q}}$ is defined by:

$$\mathrm{d}\varepsilon_{\mathrm{q}} = \sqrt{\frac{2}{3}\mathrm{d}e_{\mathrm{ij}}\mathrm{d}e_{\mathrm{ij}}} \tag{34}$$

Generalization

By using the stress and strain tensors defined above, the proposed model can be expressed in generalized forms:

1. Yield function

$$f = \frac{p}{3p_0'} - \frac{\left(1 + \frac{3q}{MpK_2}\right)^{\frac{K_2}{(1-\mu)(K_1-K_2)}}}{\left(1 + \frac{3q}{MpK_1}\right)^{\frac{K_1}{(1-\mu)(K_1-K_2)}}} = 0 \tag{35}$$

In Eq. (35), the stress ratio at critical state (M), is expressed as a function of the Lode angle θ (Sheng et al. 2000; Yin et al. 2013):

$$M = M_c \left(\frac{2\alpha^4}{1 + \alpha^4 - (1 - \alpha^4)\sin\theta} \right)^{1/4} \tag{36}$$

where M_c is the critical state stress ratio under triaxial compression ($\theta = 30^{\circ}$). The parameter $\alpha$is equal to:

$$\alpha = \frac{3 - \sin\phi'}{3 + \sin\phi'} \tag{37}$$

where the parameter ϕ' is the effective angle of shearing resistance at the critical state.

2. Hardening law and plastic modulus

$$dp_0' = \frac{(1 + e_{w0})}{\lambda - \kappa} p_0' d\varepsilon_v^p \tag{38}$$

The plastic shear strain increment is expressed as:

$$de_{ij}^p = \langle L \rangle \left[\frac{\partial f}{\partial \sigma_{ij}'} - \frac{1}{3} \frac{\partial f}{\partial \sigma_{ii}'} \delta_{ij} \right] = \langle L \rangle n_{ij} \tag{39a}$$

$$d\varepsilon_q^p = \langle L \rangle \sqrt{\frac{2}{3} n_{ij} n_{ij}} \tag{39b}$$

The plastic volumetric strain increment can be expressed as:

$$d\varepsilon_v^p = d\varepsilon_{ii}^p = \langle L \rangle \sqrt{\frac{2}{3} n_{ij} n_{ij}} D \tag{40}$$

The total plastic strain increment $d\varepsilon_{ij}^p$ can be obtained based on the basis of Eqs. (39a) and (40) as below:

$$\mathrm{d}\varepsilon_{\mathrm{ij}}^{\mathrm{p}} = \mathrm{d}e_{\mathrm{ij}}^{\mathrm{p}} + \tfrac{1}{3}\mathrm{d}\varepsilon_{\mathrm{v}}^{\mathrm{p}}\delta_{\mathrm{ij}} = \langle L\rangle\left(n_{\mathrm{ij}} + \tfrac{1}{3}\sqrt{\tfrac{2}{3}n_{\mathrm{ab}}n_{\mathrm{ab}}}D\delta_{\mathrm{ij}}\right)=\langle L\rangle m_{\mathrm{ij}} \tag{41}$$

By combining Eqs. (38) and (40) with Eq. (18), the generalized form of the plastic modulus can be obtained:

$$K_{\mathrm{p}} = -\frac{1}{L}\frac{\partial f}{\partial p_0'}\frac{\partial p_0'}{\partial \varepsilon_{\mathrm{v}}^{\mathrm{p}}}\mathrm{d}\varepsilon_{\mathrm{v}}^{\mathrm{p}} = -\frac{(1+e_{\mathrm{w0}})p_0'}{\lambda-\kappa}\frac{\partial f}{\partial p_0'}\sqrt{\frac{2}{3}n_{\mathrm{ij}}n_{\mathrm{ij}}}D \tag{42}$$

With a known K_{p}, the loading index L can be readily derived through standard elasto–plasticity procedures, as follows:

$$L = \frac{\frac{\partial f}{\partial \sigma_{\mathrm{kl}}'}C_{\mathrm{klij}}\mathrm{d}\varepsilon_{\mathrm{ij}}}{K_{\mathrm{p}} + \frac{\partial f}{\partial \sigma_{\mathrm{ab}}'}C_{\mathrm{abcd}}m_{\mathrm{cd}}} = \Pi_{\mathrm{ij}}\mathrm{d}\varepsilon_{\mathrm{ij}} \tag{43}$$

where C_{ijkl} is the elastic stiffness matrix expressed as:

$$C_{\mathrm{ijkl}} = (K - 2G/3)\delta_{ij}\delta_{kl} + G(\delta_{ki}\delta_{lj} + \delta_{li}\delta_{kj}) \tag{44}$$

where $\frac{\partial f}{\partial \sigma_{\mathrm{ij}}'}$ can be expressed as:

$$\frac{\partial f}{\partial \sigma_{\mathrm{ij}}'} = \frac{\partial f}{\partial p'}\frac{\partial p'}{\partial \sigma_{\mathrm{ij}}'} + \frac{\partial f}{\partial q}\frac{\partial q}{\partial \sigma_{\mathrm{ij}}'} = \frac{1}{3}\frac{\partial f}{\partial p'}\delta_{\mathrm{ij}} + \frac{3}{2q}\frac{\partial f}{\partial q}s_{\mathrm{ij}} \tag{45}$$

3. Elasto–plastic relation

The generalized incremental elastoplastic relation can be derived as follows:

$$\begin{aligned}\mathrm{d}\sigma_{\mathrm{ij}}' &= C_{\mathrm{ijkl}}\left(\mathrm{d}\varepsilon_{\mathrm{kl}} - \mathrm{d}\varepsilon_{\mathrm{kl}}^{\mathrm{p}}\right) = C_{\mathrm{ijkl}}(\mathrm{d}\varepsilon_{\mathrm{kl}} - \langle L\rangle m_{kl}) \\ &= \left(C_{\mathrm{ijkl}} - h(L)C_{\mathrm{ijab}}m_{ab}\Pi_{kl}\right)\mathrm{d}\varepsilon_{kl} = D_{\mathrm{ijkl}}\mathrm{d}\varepsilon_{kl}\end{aligned} \tag{46}$$

Acknowledgements

The authors gratefully acknowledge the financial supports from the National Key Research and Development Program (Grant No. 2016YFC0800200), National Natural Science Foundation of China (51779221), the Key Research and Development Program of Zhejiang Province (2018C03031) and Qianjiang Talent Plan (QJD1602028). The valuable comments given by Professor Simon Wheeler in University of Glasgow are gratefully acknowledged.

Notation

The following symbols are used in this paper:

$a, b =$ Parameters controling the shape of yield curve;

$D =$ stress–dilatancy function;

$\mathrm{d}u_{\mathrm{g}} =$ increment of pore gas pressure;

$\mathrm{d}V_{\mathrm{g}} =$ increment of gas volume;

$\mathrm{d}\varepsilon_{ij}, \mathrm{d}\varepsilon_{ij}^{\mathrm{e}}, \mathrm{d}\varepsilon_{ij}^{\mathrm{p}} =$ increment of total, elastic and plastic strain, respectively;

$\mathrm{d}\varepsilon_{\mathrm{v}}, \mathrm{d}\varepsilon_{\mathrm{v}}^{\mathrm{e}}, \mathrm{d}\varepsilon_{\mathrm{v}}^{\mathrm{p}} =$ increment of total, elastic and plastic volumetric strain, respectively;

$\mathrm{d}\varepsilon_{\mathrm{q}}, \mathrm{d}\varepsilon_{\mathrm{q}}^{\mathrm{e}}, \mathrm{d}\varepsilon_{\mathrm{q}}^{\mathrm{p}} =$ increment of total, elastic and plastic deviatoric strain, respectively;

$\mathrm{d}\varepsilon_1, \mathrm{d}\varepsilon_3 =$ increment of major and minor principle strain;

$\mathrm{d}\varepsilon_{\mathrm{v}}^{\mathrm{g}} =$ the volumetric strain increment of gas;

$e_{\mathrm{w}} =$ void ratio of saturated matrix;

$f =$ yield function;

$F =$ dilatancy multiplier;

$G =$ elastic shear modulus of saturated matrix;

$K =$ elastic bulk modulus of saturated matrix;

$K_{1/2} =$ constant of yield function;

$K_{\mathrm{p}} =$ plastic modulus;

$L =$ loading index;

$M =$ stress ratio at critical state;

$N =$ intercept of normally consolidated line;

$n_{\mathrm{g}} =$ the number of the mole of the gas;

$p_{\mathrm{a}} =$ atmospheric pressure;

$p'_0 =$ pre–consolidation pressure;

$p' =$ effective mean stress;

$p'_{\mathrm{i}} =$ current effective mean pressure;

$p'_{\mathrm{y}}, q_{\mathrm{y}} =$ effective mean stress and deviatoric stress at onset of yielding

$q =$ deviatoric stress;

$R =$ ideal gas constant;

$S_{\mathrm{r}} =$ degree of saturation;

$s_{\mathrm{u}} =$ undrained shear strength;

$s_{\mathrm{u\_gas}}, s_{\mathrm{u\_sat}} =$ undrained shear strength of gassy soil and saturated soil, respectively;

$s_{ij} =$ deviatoric stress tensor;

$T =$ absolute temperature;

$u_{\mathrm{w0}} =$ initial pore water pressure;

$u_{\mathrm{w0\_ref}} =$ reference initial pore water pressure;

$u_{\mathrm{g}} =$ pore gas pressure;

$u_{\mathrm{g0}} =$ initial pore gas pressure;

$V_{\mathrm{g}} =$ gas volume;

$V_{\mathrm{g0}} =$ initial gas volume;

$\nu =$ Poisson's ratio;

$W =$ total strain energy;

$\psi_0 =$ initial gas volume fraction;

$\lambda =$ slope of the normally consolidated line;

$\kappa =$ slope of the swelling line;

$\eta =$ stress ratio;

$\xi, \chi =$ parameters governing the stress–dilatancy;

$\sigma_{ij} =$ stress tensor;

$\delta_{ij} =$ Kronecker delta;

$\sigma'_1, \sigma'_3 =$ major and minor principle effective stress;

$\mu, \alpha =$ parameters controling the shape of yield curve.

Superscripts

$i, j =$ 1–, 2–, or 3.

References

Abuel–Naga, H. M., D. T. Bergado, A. Bouazza, and M. Pender. 2009. “Thermomechanical model for saturated clays.” *Géotechnique* 59 (3): 273–278.

Alonso E. E., A. Gens, A. Josa. 1990. “A constitutive model for partially saturated soils.” *Géotechnique* 40 (3): 405–30.

Bishop, A.W., and D.J. Henkel. 1962. “The measurement of soil properties in the triaxial test.” 2nd Ed., Arnold, London.

BSI 1999. “BS 5930: Code of Practice for Site Investigations”. *British Standard Institution*, London.

Cekerevac, C., and L. Laloui. 2004. “Experimental study of thermal effects on the mechanical behaviour of a clay.” *Int. J. Numer. Anal. Meth. Geomech.* 28 (3):209–228.

Chen, Y. N., and Z. X. Yang. 2017. “A family of improved yield surfaces and their application in modeling of isotropically over–consolidated clays.” *Comput. Geotech.* 90: 133–143.

Collins, I. F., and T. Hilder.2002. “A theoretical framework for constructing elastic/plastic constitutive models of triaxial tests.” *Int. J. Numer. Anal. Meth. Geomech*. 25 (13): 1313–1347.

Collins, I. F. 2005. “Elastic/plastic models for soils and sands.” *Int. J. Mech. Sci*.47(4): 493–508.

Dafalias, Y. F. 1986. “An anisotropic critical state soil plasticity model.” *Mech. Res. Commun*.13 (6): 341–347.

Dafalias, Y. F., M. T. Manzari, and A. G. Papadimitriou. 2006.“SANICLAY: simple anisotropic clay plasticity model.” *Int. J. Numer. Anal. Meth. Geomech*. 30 (12): 1231–1257.

Dittrich, J P., R. K. Rowe, D. E. Becker, and K. Y. Lo. 2010. “Influence of exsolved gases on slope performance at the Sarnia approach cut to the St. Clair Tunnel.” *Can. Geotech. J.* 47 (9): 971–984.

Evans, T. G. 2011. “A systematic approach to offshore engineering for multiple–project developments in geohazardous areas.” *Proc. 2nd Int. Symp. on Frontiers in Offshore Geotechnics*, *ISFOG*, *Perth*, 3–32.

Gallipoli, D., P. Grassl, S. J. Wheeler, and A. Gens. 2018. “On the choice of stress–strain variables for unsaturated soils and its effect on plastic flow.” *Geomech Energy Envir*. 15: 3–9.

Gao, Z., J. Zhao, and Z. Y. Yin.2017. “Dilatancy relation for overconsolidated clay.” *Int. J. Geomech.*17 (5) 06016035.

Graham, J., R. B. Pinkney, K. V. Lew, and P. G. S. Trainor. 1982.“Curve fitting and laboratory data.” *Can. Geotech. J.*19 (2):201–205.

Grozic, J. L. H., P. K. Robertson, and N. R. Morgenstern. 2000.“Cyclic liquefaction of loose gassy sand.” *Can. Geotech. J.* 37 (4): 843–856.

Grozic, J. L. H., F. Nadim, and T. J. Kvalstad.2005. “On the undrained shear strength of gassy clays.” *Comput. Geotech*. 32 (7): 483–490.

Hight, D. W.,and S. Leroueil.2003. “Characterisation of soils for engineering purposes.” In *Characterisation and engineering properties of natural soils* (eds T. S Tan, K. K. Phoon, D. W. Hight and S. Leroueil), pp. 255–362. Lisse, the Netherlands: Balkema.

Hong, Y., L. Z. Wang, C. W. W. Ng, and B. Yang.2017. “Effect of initial pore pressure on undrained shear behaviour of fine–grained gassy soil.” *Can. Geotech. J.*54 (11): 1592–1600.

Hong, Y., L. Z. Wang, B. Yang, and J. F. Zhang. 2019b. “Stress–dilatancy behaviour of bubbled fine–grained sediments.” *Eng. Geol.*26 (3): 105196.

Hong, Y., J. F. Zhang, L. Z. Wang, and T. Liu. 2019a. “On evolving size and shape of gas bubble in marine clay under multi–stage loadings: μCT characterization and cavity contraction analysis.” *Can. Geotech. J.* under review

Huang, M., Y. Liu, and D. Sheng.2011. “Simulation of yielding and stress–strain behaviour of shanghai soft clay.” *Comput. Geotech*. 38 (3): 341–353.

Jiang, J., and H. I. Ling. 2010. “A framework of an anisotropic elastoplastic model for clays.” *Mech. Res. Commun.*37 (4): 394–398.

Kortekaas, S., and J. Peuchen.2008. “Measured swabbing pressures and implications for shallow gas blow–out.” *Proc. Offshore Technol. Conf.*, *Houston*, *TX*, paper OTC 19280.

Kvenvolden, K. A. 1988. “Methane hydrate—A major reservoir of carbon in the shallow geosphere?” *Chemical Geology*.71 (1–3): 41–51.

Lagioia, R., A. M. Puzrin, and D. M. Potts.1996. “A new versatile expression for yield and plastic potential surfaces.” *Comput. Geotech*. 19 (3): 171–191.

Lin, C. M., L. X. Gu, G. Y. Li, Y. Y. Zhao, and W. S. Jiang. (2004). “Geology and formation mechanism of late Quaternary shallow biogenic gas reservior in the Hangzhou bay area, Eastern China.” *AAPG Bulletin*. 98(5): 613–625.

Ling, H. I., D. Yue, V. N. Kaliakin, and N. J. Themelis.2002. “Anisotropic elastoplastic bounding surface model for cohesive soils.” *J. Eng. Mech.*128 (7): 748–758.

Locat, J., and H. J. Lee.2002. “Submarine landslides: advances and challenges.” *Can. Geotech. J.* 39 (1): 193–212.

Lunne, T., T. Berre, S. Stranvik, K. H. Andersen, and, T. I. Tjelta.2001. “Deepwater sample disturbance due to stress relief.” In Proceedings of the OTRC 2001 International Conference, Houston, Tex. pp. 64–85.

Matsuoka, H., Y. P. Yao, and D. A. Sun.1999. “The cam–clay models revised by the SMP criterion.” *Soils Found*.39 (1): 81–95.

Milich, L. 1999. “The role of methane in global warming: where might mitigation strategies be focused?” *Global Environmental Change*.9 (3): 179–201.

Nageswaran, S. 1983. “Effect of gas bubbles on the seabed behaviour.” Ph.D. thesis, Oxford University.

Ng, C.W.W., L.T. Zhan, and Y.J. Cui. 2002. “A new simple system for measuring volume changes in unsaturated soils.” *Can. Geotech. J.* 39(3):757–764.

Nisbet, E. G., and D. J. Piper. 1998. “Giant submarine landslides.” *Nature.* 392 (6674): 329–330.

Pestana, J. M., and A. J. Whittle. 1999. “Formulation of a unified constitutive model for clays and sands.” *Int. J. Numer. Anal. Meth. Geomech*. 23 (1):1215–1243.

Pestana, J. M., A. J. Whittle, and A. Gens.2002. “Evaluation of a constitutive model for clays and sands: Part II – clay behaviour.” *Int. J. Numer. Anal. Meth. Geomech.* 26 (11): 1123–1146.

Pietruszczak, S., and G. N. Pande. 1996. “Constitutive relations for partially saturated soils containing gas inclusions.” *J. Geotech. Engng*, *ASCE*122 (1): 50–59.

Puzrin, A. M., J. Tront, A. Schmid, and J. B. Hughes. 2011. “Engineered use of microbial gas production to decrease primary consolidation settlement in clayey soils.” *Géotechnique* 61 (9): 785–794.

Rebata–Landa, V., and J. C. Santamarina.2012. “Mechanical effects of biogenic nitrogen gas bubbles in soils.” *J. Geotech. Geoenviron. Engng*.138 (2): 128–137.

Roscoe, K. H., and J. B. Burland.1968. “On the generalized stress–strain behaviour of ‘wet clay’.” In *Engineering plasticity* (eds J. Heyman and F. A. Leckie), pp. 535–609. Cambridge: Cambridge University Press.

Rowe, R. K., and A. Mabrouk. 2012. “Forensic numerical analysis of gas venting in Southwestern Ontario.” *Eng. Geol.*151 (4): 47–55.

Sham, W. K. 1989. “The undrained shear strength of soils containing large gas bubbles.” Ph.D. thesis, Queen's University of Belfast, UK.

Sheng, D., S. W. Sloan, and H. S. Yu.2000. “Aspects of finite element implementation of critical state models.” *Comput. Mech.* 26 (2):185–196.

Sills, G. C., S. J. Wheeler, S. D. Thomas, and T. N. Gardner.1991. “Behaviour of offshore soils containing gas–bubbles.”*Géotechnique*41 (2): 227–241.

Sparks, A. D. W. 1963. “Theoretical considerations of stress equations for partly saturated soils.” Proceedings of the 3rd African conference on soil mechanics and foundation engineering, Salisbury, Rhodesia, vol. 1, pp. 215–218. Rotterdam, the Netherlands: Balkema.

Sultan, N., V. De Gennaro, and A. Puech.2012. “Mechanical behaviour of gas–charged marine plastic sediments.” *Géotechnique* 62 (9): 751–766.

Sultan, N., and S. Garziglia. 2014. "Mechanical behaviour of gas–charged fine sediments: model formulation and calibration." *Géotechnique* 64 (11): 851–864.

Sun, D. A., H. Matsuoka, Y. P. Yao, W. Ichihara. 2000. "An elasto–plastic model for unsaturated soil in three–dimensional stresses." *Soils Found*, 40(3): 17–28.

Thomas, S. D. 1987. "The consolidation behaviour of gassy soil." Ph.D. thesis, Oxford University.

Thomas, S. D., M. Clare, J. Shreeve, and S. Unterseh.2011. "Understanding engineering challenges posed by natural hydrocarbon infiltration and the development of authigenic carbonate." *Proc. Offshore Technol. Conf.*, *Houston*, *TX*, paper OTC 21253.

Wang, L. Z., H. B. Dan, and L. L. Li. 2012. "Modeling strain–rate dependent behaviour of KR_0–consolidated soft clays." *J. Eng. Mech.*138 (7): 738–748.

Wang, L. Z., K. J. Wang, and Y. Hong.2016. "Modeling temperature–dependent behaviour of soft clay." *J. Eng. Mech.* 142 (8): 04016054.

Wang, L. Z., Y. Hong, and J. F. Zhang.2018. "Laboratory testing on the mechanical behaviour of fine–grained gassy and saturated soil in Zhoushan, China." Internal Report.

Wheeler, S. J. 1986. "The stress–strain behaviour of soils containing gas bubbles." Ph.D. thesis, Oxford University.

Wheeler, S. J. 1988a. "A conceptual model for soils containing large gas bubbles." *Géotechnique* 38 (3): 389–397.

Wheeler, S. J. 1988b. "The undrained shear strength of soils containing large gas bubbles." *Géotechnique* 38 (3): 399–413.

Wheeler, S. J., A. Näätänen, M. Karstunen, and M. Lojander.2003. "An anisotropic elastoplastic model for soft clays." *Can. Geotech. J.*40 (2): 403–418.

Wheeler, S. J., W. K. Sham, and S. D. Thomas.1990. "Gas pressure in unsaturated offshore soils." *Can. Geotech. J.* 27 (1): 79–89.

Wood, D. 1991. "Soil behaviour and critical state soil mechanics." Cambridge: Cambridge University Press.

Xu, H.F., and K.H. Xie.2011. "Effective stress in soils under different saturation conditions." *J. Cent. South Univ. Technol*. 18: 2137–2142.

Xu, Y.S., S. L. J. Shen, A. N. Zhou, and A.Arulrajah.2018. "Geological and hydrogeological environment with geohazards during underground construction in Hangzhou: a review." 11: 544.

Yao, Y., Z. Gao, J. Zhao, and Z. Wan.2012. "Modified UH model: constitutive modeling of overconsolidated clays based on a parabolic hvorslev envelope." *J. Geotech. Geoenviron. Eng.*138 (7): 860–868.

Yang, Z. X., C. F. Zhao, C. J. Xu, S. P. Wilkinson, Y. Q. Cai, and K. Pan. 2016. Modelling the engineering behaviour of fibrous peat formed due to the rapid anthropogenic terrestrialization in Hangzhou, China. *Eng. Geo.* 215: 25–35.

Yin, J. H., J. G. Zhu, and J. Graham.2002. “A new elastic viscoplastic model for time–dependent behaviour of normally and overconsolidated clays: theory and verification.” *Can. Geotech. J.*39 (1): 157–173.

Yin, Z. Y., and C. S. Chang.2009. “Non‐uniqueness of critical state line in compression and extension conditions.” *Int. J. Numer. Anal. Meth. Geomech.* 33 (10): 1315–1338.

Yin, Z. Y., Q. Xu, and P. Y. Hicher.2013. “A simple critical–state–based double–yield–surface model for clay behaviour under complex loading.” *Acta Geotech.* 8 (5):509–523.

Yu, H. S. 1998. “CASM: a unified state parameter model for clay and sand.” *Int. J. Numer. Anal. Meth. Geomech*. 22 (8): 621–653.

Zhou, A. N., and D. C. Sheng. 2015.“An advanced hydro–mechanical constitutive model for unsaturated soils with different initial densities.” *Comput. Geotech*. 63: 46–66.

Zhou, C., and C. W. W. Ng.2016. “Simulating the cyclic behaviour of unsaturated soil at various temperatures using a bounding surface model.” *Géotechnique*, 66 (4): 344–350.

Caption of Tables

Table 1. Program of test series I (for studying yield function and flow rule).

Table 2. Program of test series II (for proposing shape- and dilatancy-related functional forms) (Hong et al. 2019b).

Table 3. Index properties of Malaysia Kaolin silt.

Table 4. Yield stress from different yield criteria.

Table 5. Angle between plastic strain increment vector and the normal to the yield envelope.

Table 6. Model parameters of three type of fine-grained gassy soils.

Table 1. Program of test series I (for studying yield function and flow rule).

	Specimen identity	Amount of nitrogen, m: 1×10^{-4} mol	Initial pore water pressure, u_{w0}: kPa	After consolidation: Pre-consolidation pressure, p'_0: kPa	Gas volume fraction*, ψ : %	Degree of saturation*, S_r : %	After unloading: Current consolidation pressure, p'_i: kPa	OCR	Degree of saturation*, S_r : %
Group A	G0_120	4.6	0	200	6.3	89.7	120	1.67	89.9
	G0_140				5.9	90.1	140	1.43	90.2
	G0_160				6.7	89.0	160	1.25	89.1
	G0_170				5.7	90.5	170	1.18	90.6
	G0_180				5.5	90.8	180	1.11	90.8
	G0_190				6.3	89.5	190	1.05	89.5
Group B	G150_120		150		3.6	94.1	120	1.67	94.2
	G150_140				3.9	93.5	140	1.43	93.6
	G150_160				3.5	94.2	160	1.25	94.2
	G150_170				3.7	93.8	170	1.18	93.8
	G150_180				3.3	94.5	180	1.11	94.5
	G150_190				3.6	94.0	190	1.05	94.0
Group C	G600_120		600		2.5	95.9	120	1.67	96.0
	G600_140				2.3	96.2	140	1.43	96.2
	G600_160				2.6	95.7	160	1.25	95.7
	G600_170				2.4	96	170	1.18	96.0
	G600_180				2.1	96.5	180	1.11	96.5
	G600_190				2.3	96.1	190	1.05	96.1
Group D	S300_120	0	300		0	100	120	1.67	100
	S300_140						140	1.43	
	S300_160						160	1.25	
	S300_170						170	1.18	
	S300_180						180	1.11	
	S300_190						190	1.05	

Table 2. Program of test series II (for proposing shape- and dilatancy-related functional forms) (Hong et al. 2019b).

Specimen type ┼	Specimen identity	Initial pore water pressure*, u_{w0} : kPa	Initial water void ratio*, e_{w0}	Initial degree of saturation*, S_{r0} : %	Initial gas volume fraction*, ψ : %	Percentage of zeolite saturated with nitrogen: %	Amount of nitrogen, m: 1×10^{-4} mol
Gassy	G0_89.7	0	1.35	89.7	6.3	100	4.6
	G0_92.1		1.36	92.1	4.8	75	3.5
	G0_94.6		1.34	94.8	3.3	50	2.3
	G0_96.9		1.37	96.5	1.9	25	1.2
	G50_93.5	50	1.34	93.5	4.2	100	4.6
	G50_94.6		1.35	94.6	3.3	75	3.5
	G50_96.2		1.36	96.2	2.4	50	2.3
	G50_97.8		1.37	97.8	1.4	25	1.2
	G150_94.1	150	1.35	94.1	3.6	100	4.6
	G150_97.0		1.37	97.0	1.9	50	2.3
	G300_95.2	300	1.36	95.2	3.0	100	4.6
	G300_96.2		1.35	96.2	2.3	75	3.5
	G300_97.5		1.37	97.5	1.6	50	2.3
	G300_98.5		1.36	98.5	1.0	25	1.2
	G600_95.9	600	1.35	95.9	2.5	100	4.6
	G600_96.6		1.36	96.6	2.1	75	3.5
	G600_97.9		1.34	97.9	1.3	50	2.3
	G600_99.0		1.36	99.0	0.6	25	1.2
Saturated	S300_100	300	1.38	100.0	0	0	0

┼: The pre-consolidation pressure (p'_0) of each specimen is 200 kPa.

*: Each initial value is corresponding to the stage immediately before the undrained triaxial shearing.

Table 3. Index properties of Malaysia Kaolin silt.

Index property	Value
Atterberg limits	
Liquid limit: %	65
Plastic limit: %	38
Plasticity index	27
Grain size distribution	
Percentage of sand: %	0
Percentage of silt: %	35.1
Percentage of clay: %	64.9

Table 4. Yield stress from different yield criteria.

Current consolidation pressure: kPa	**Gassy specimen**												**Saturated specimen**			
	u_{w0}=0 kPa				**u_{w0}=150 kPa**				**u_{w0}=600 kPa**				**u_{w0}=300 kPa**			
	q vs ε_q		**W vs q/p'**		**q vs ε_q**		**W vs q/p'**		**q vs ε_q**		**W vs q/p'**		**q vs ε_q**		**W vs q/p'**	
	p'_y	q_y	p'_y	q_y	p'_y	q_y	p'_y	q_y	p'_y	q_y	p'_y	q_y	p'_y	q_y	p'_y	q_y
190	192	100	191	99	192	44	186	48	195	25	191	27	193	43	190	37
180	179	138	183	142	179	58	178	61	183	36	176	41	179	66	182	70
170	171	155	168	157	172	76	168	72	170	42	172	38	169	77	173	79
160	157	159	161	162	158	95	160	97	159	46	158	52	163	82	162	78
140	142	152	139	148	141	100	143	100	141	60	138	59	139	91	140	93
120	123	144	120	145	120	104	116	106	125	81	119	79	118	110	121	108

Note: p'_y and q_y denotes the mean effective stress and deviatoric stress at yield, respectively.

Table 5. Angle between plastic strain increment vector and the normal to the yield envelope.

Current consolidation pressure: kPa	**Angle between plastic strain increment vector and normal to the yield envelope, α: °**			
	Gassy specimen			**Saturated specimen**
	u_{w0}=0 kPa	**u_{w0}=150 kPa**	**u_{w0}=600 kPa**	**u_{w0}=300 kPa**
190	-68	2	31	2
180	-58	0	36	1
170	-41	-1	37	-2
160	-18	-2	36	-3
140	18	-3	36	-4
120	35	-3	32	-5

Note: $\alpha = 0^\circ$ means the normality rule holds.

Table 6. Model parameters of three type of fine-grained gassy soils.

	Meaning of parameters	Parameter	Malaysia kaolin silt (Hong et al., 2017)	Combwich mud (Wheeler, 1986)	Kaolin clay (Sham, 1989)
MCC parameters	Slope of compression line in $e_{\mathrm{w}} - \ln p'$ plane	$\boldsymbol{\lambda}$	0.24	0.174	0.23
	Slope of swelling line in $e_{\mathrm{w}} - \ln p'$ plane	$\boldsymbol{\kappa}$	0.05	0.035	0.046
	Intercept of NCL in $e_{\mathrm{w}} - \ln p'$ plane	$\boldsymbol{N}$	2.74	3.062	3.35
	Stress ratio at the critical state	$\boldsymbol{M}$	1.05	1.33	0.9
	Poission's ratio	$\boldsymbol{v}$	0.3	0.3	0.3
New parameters in this model	Shape parameters of yield surface	$\boldsymbol{a}$	0.16	0.2	0.5
		$\boldsymbol{b}$	0.33	0.1	-0.1
	Parameters of dilatancy function	$\boldsymbol{\xi}$	1.5	1.3	1.1
		$\boldsymbol{\chi}$	0.02	0.016	0.01
	Parameter of initial gas pressure	$\boldsymbol{\delta}$	0.7	0.6	N/A*

*: the parameter δ for Kaolin clay is not available, as the compression curves were not reported by Sham (1989).

Caption of Figures

Fig. 1. Micro-structure of a typical fine-grained gassy soil (Hong et al., 2019a): (a) micro-computed tomography (μCT) image; (b) scanning electron microscopy (SEM) image.

Fig. 2. The loci of effective stress path due to undrained triaxial compression on gassy Malaysian kaolin (data from Hong et

Fig. 3. (a) A representative volume element (RVE) of fine-grained gassy soil; (b) phase diagram and governing equations for the saturated matrix and gas.

Fig. 4. Varying shapes of yield surface with different values of shape parameter α: (a) in $p' - q$ space; (b) in $p' - q - e_{\mathrm{w}}$

Fig. 5. Identification of the yield point based on different criteria: (a)-(c) deviatoric stress vs axial strain; (e)-(f) dissipated strain energy vs q/p'.

Fig. 6. Normalized yield envelopes of gassy Malaysian kaolin (with different u_{w0} and ψ_0) and incremental plastic strain vectors.

Fig. 7. Comparison between the measured and predicted dilatancy multiplier *F* for all the tests (in Series I and II).

Fig. 8. Comparison between the measured and predicted shape parameter α for all the tests (in Series I and II).

Fig. 9. Correlating the four new model parameters to the liquid limit (LL) of three types of fine-grained gassy soil.

Fig. 10. Comparison between the predicted and measured compression behavior of (a) gassy Combwich mud (data from Thomas 1987); (b) gassy Malaysia Kaolin silt (data from Hong et al. 2017).

Fig. 11. Comparison between the predicted and measured shear behavior of gassy Malaysia Kaolin silt (data from Hong et al. 2019b): (a) stress-strain relation; (b) pore pressure response; (c) effective stress path.

Fig. 12. Comparison between the predicted and measured shear behavior of gassy Combwich mud (data from Wheeler 1986): (a) stress-strain relation; (b) pore pressure response; (c) effective stress path.

Fig. 13. Comparison between the predicted and measured shear behavior of gassy Kaolin clay (data from Sham 1989): (a) stress-strain relation; (b) effective stress path.

Fig. 14. Comparison between the predicted and measured undrained shear strength of gassy Malaysia Kaolin silt (data from Hong et al. 2019b).

Fig. 15. Comparison between the predicted and measured undrained shear strength of gassy Combwich mud (data from Wheeler 1986).

Fig. 16. Comparison between the predicted and measured undrained shear strength of gassy Kaolin clay (data from

Fig. 17. Calculation chart for quantifying the s_u of gassy soils: (a) Malaysia kaolin silt; (b) Combwich mud; (c) Kaolin clay

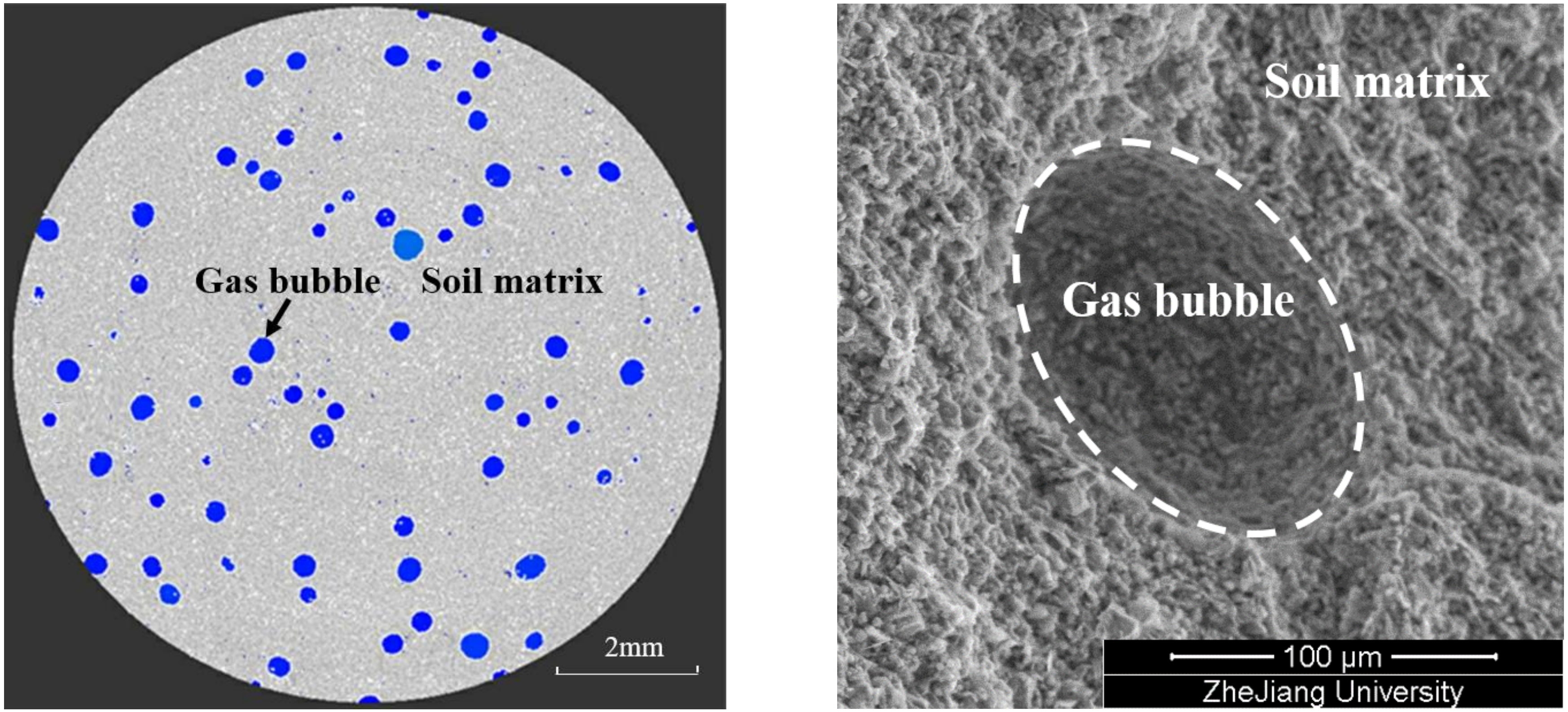

(a) (b)

Fig. 1. Micro-structure of a typical fine-grained gassy soil (Hong et al., 2019a): (a) micro-computed tomography (μCT) image; (b) scanning electron microscopy (SEM) image.

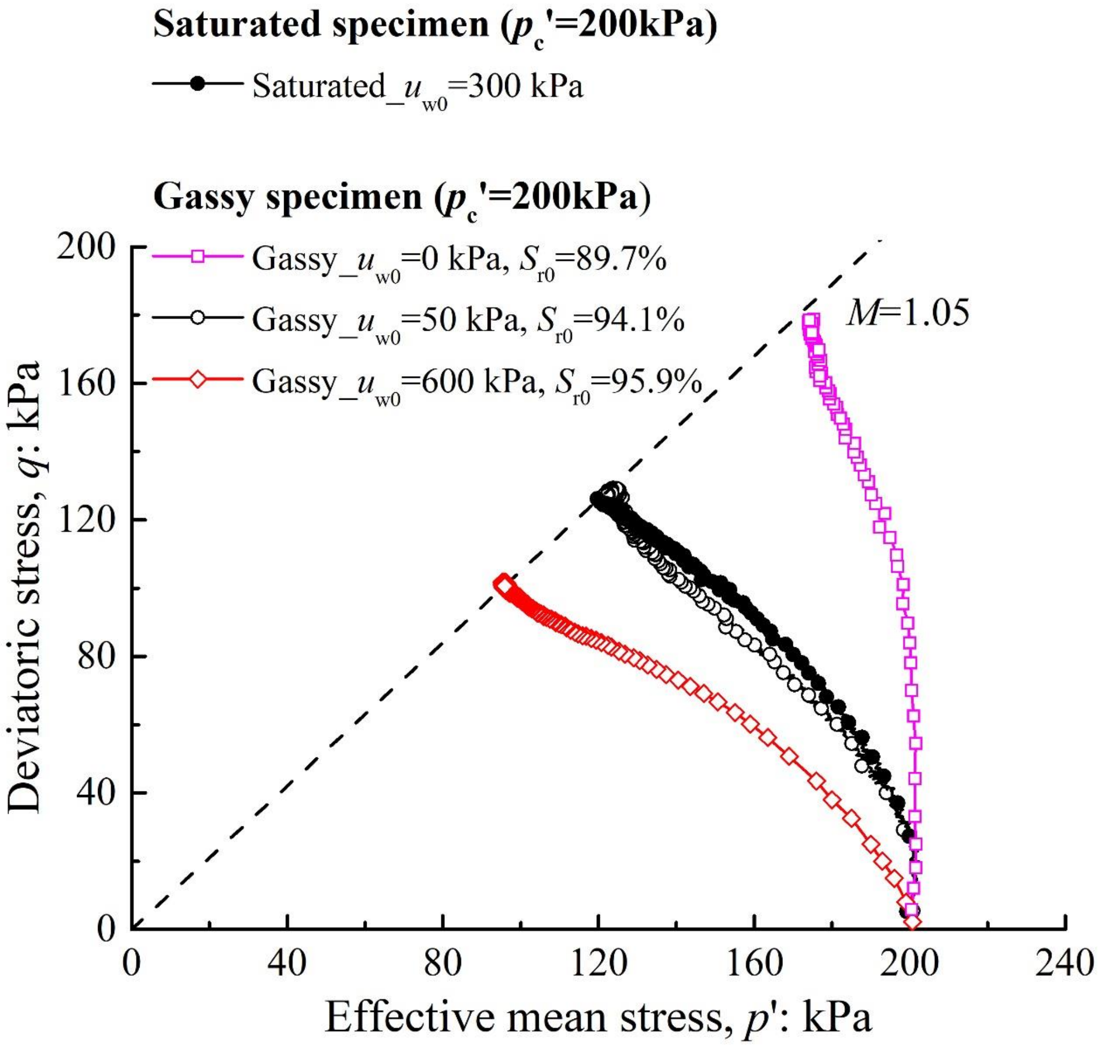

Fig. 2. The loci of effective stress path due to undrained triaxial compression on gassy Malaysian kaolin (data from Hong et al. 2019b).

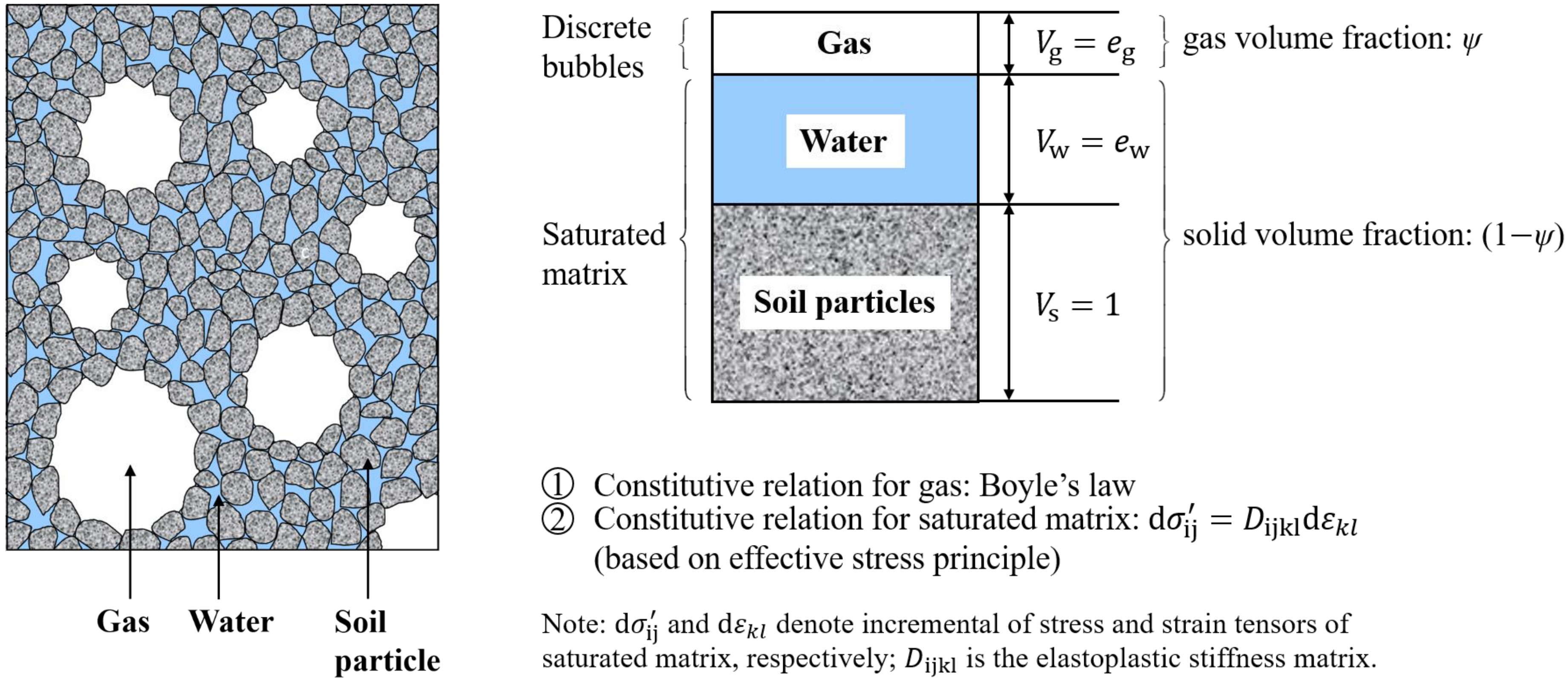

(a) (b)

Fig. 3. (a) A representative volume element (RVE) of fine-grained gassy soil; (b) phase diagram and governing equations for the saturated matrix and gas.

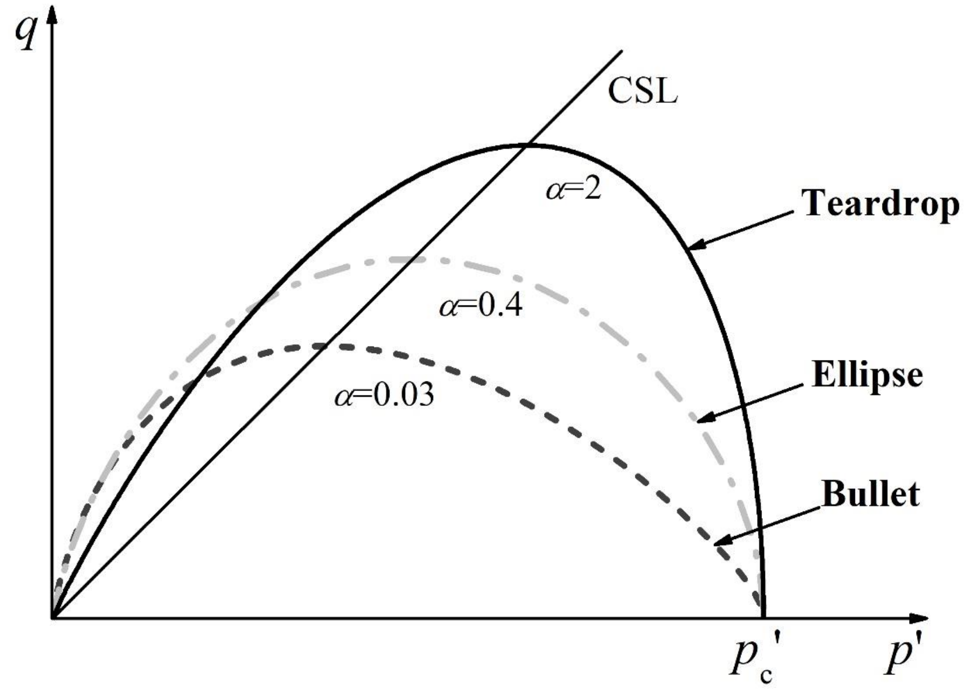

(a)

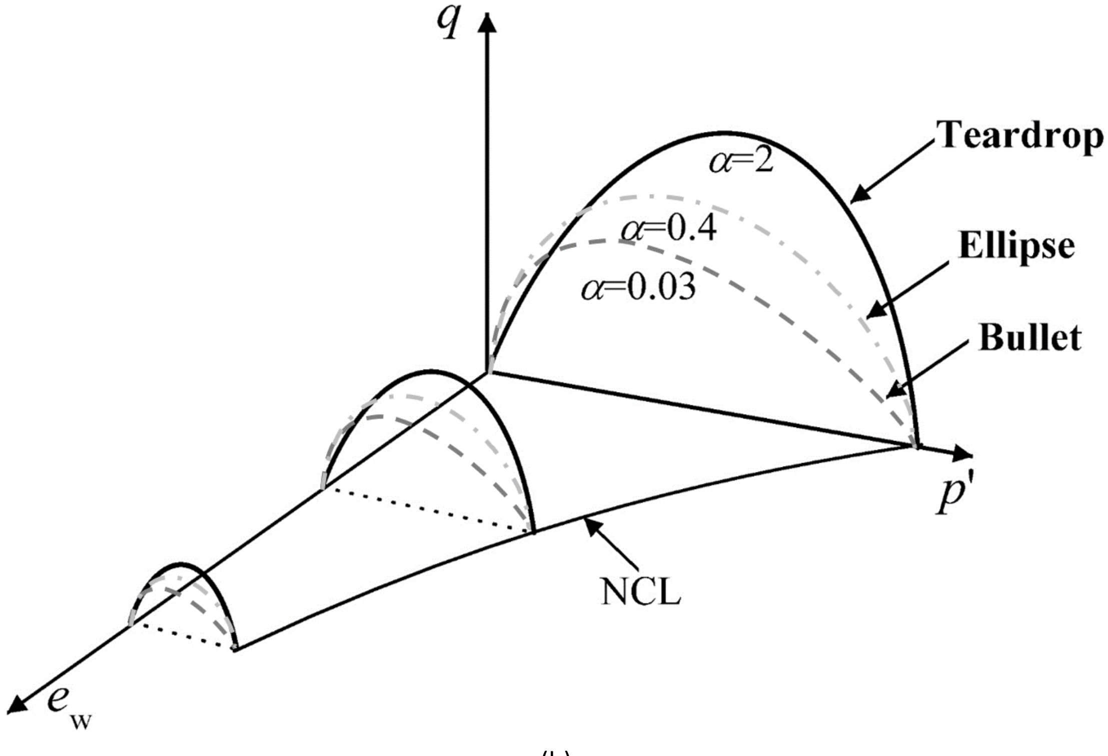

(b)

Fig. 4. Varying shapes of yield surface with different values of shape parameter α: (a) in $p' - q$ space; (b) in $p' - q - e_{\mathrm{w}}$ space.

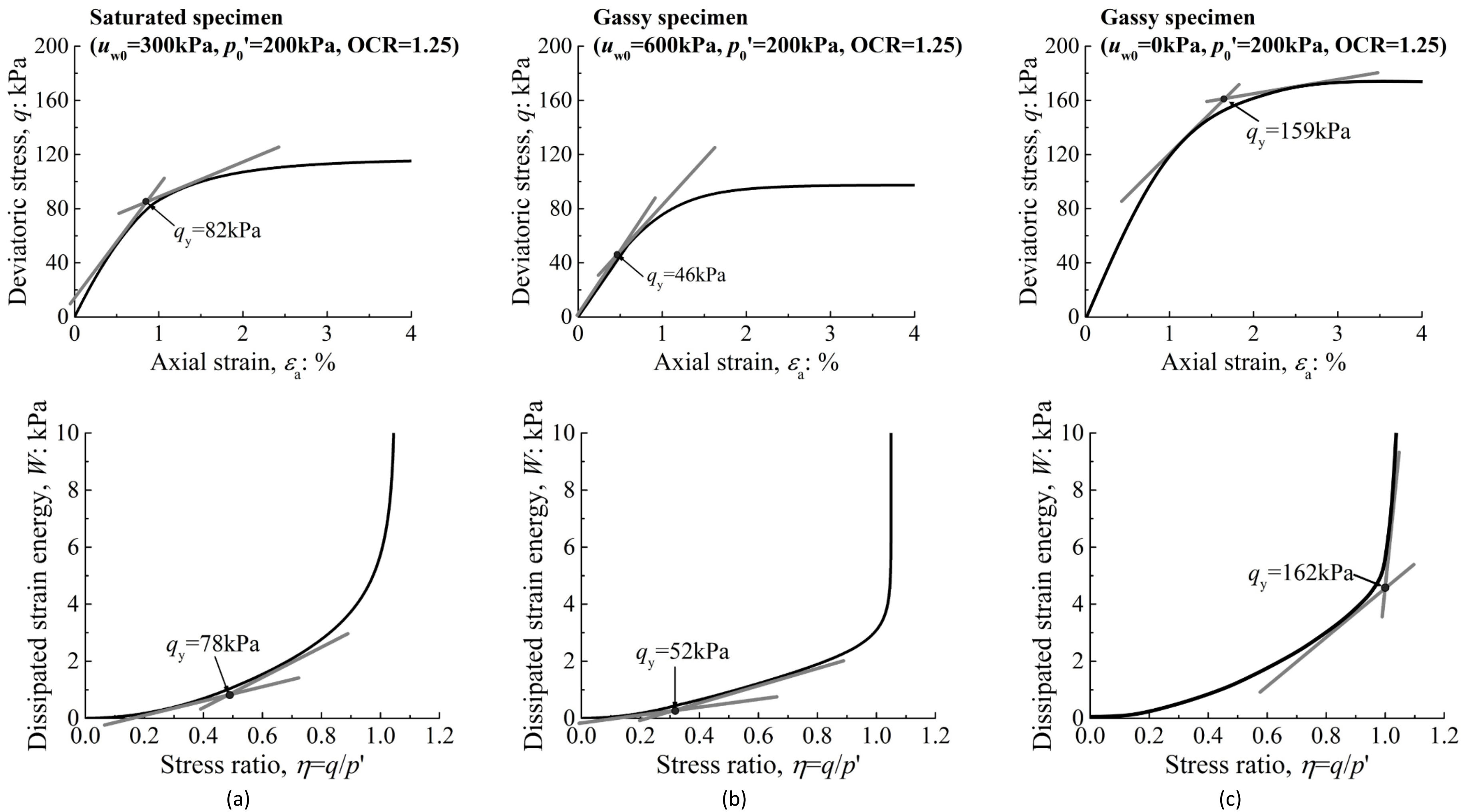

Fig. 5. Identification of the yield point based on different criteria: (a)-(c) deviatoric stress vs axial strain; (e)-(f) dissipated strain energy vs q/p'.

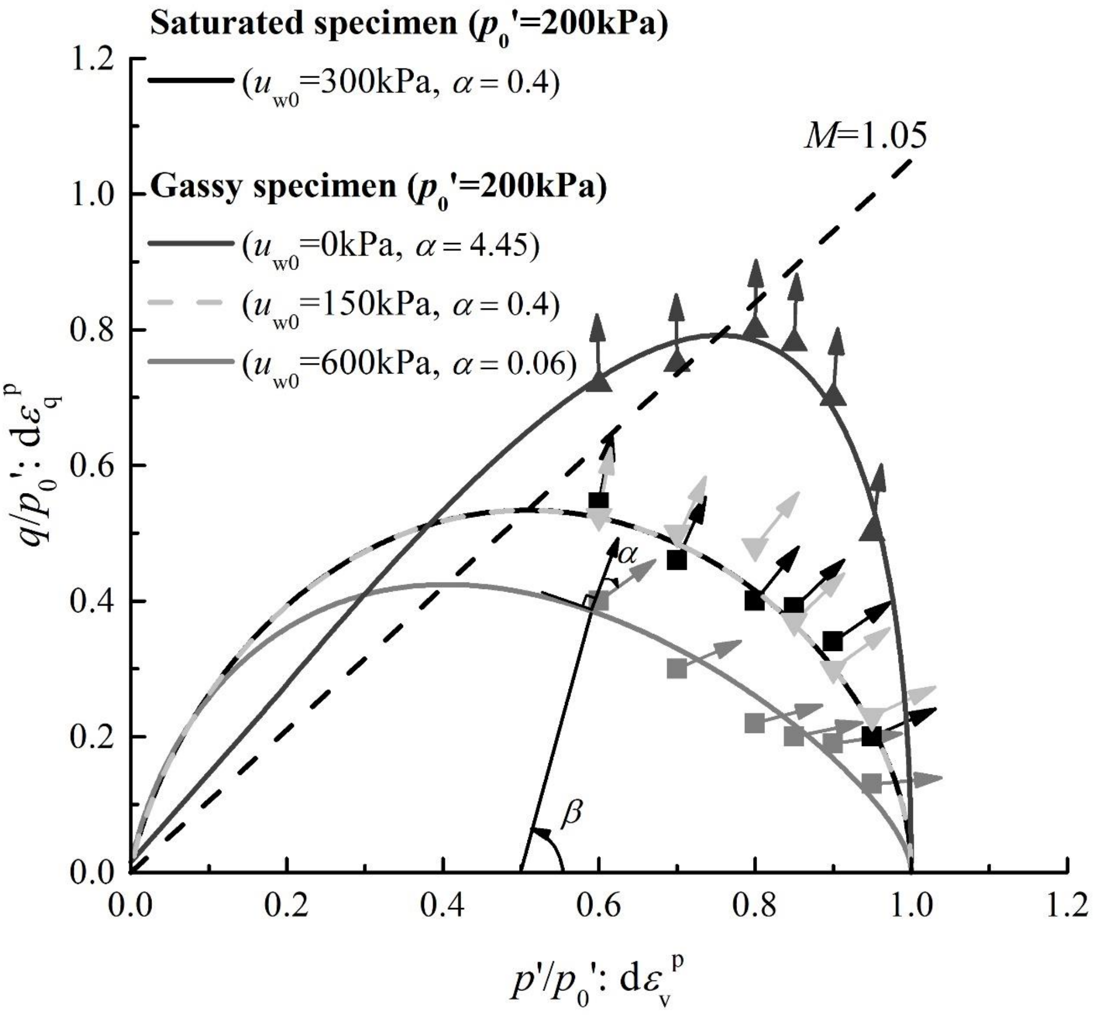

Fig. 6. Normalized yield envelopes of gassy Malaysian kaolin (with different u_{w0} and ψ_0) and incremental plastic strain vectors.

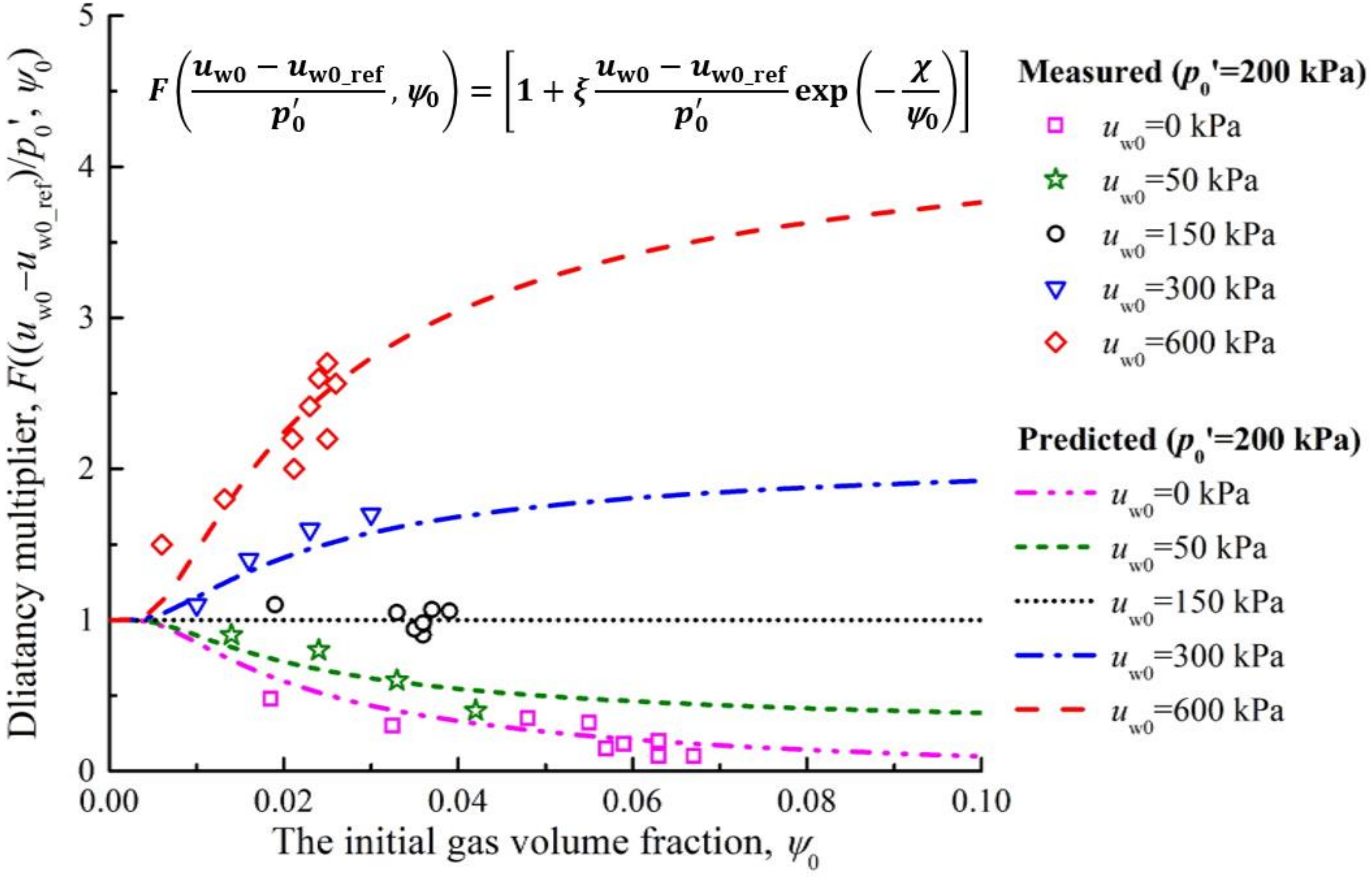

Fig. 7. Comparison between the measured and predicted dilatancy multiplier F for all the tests (in Series I and II).

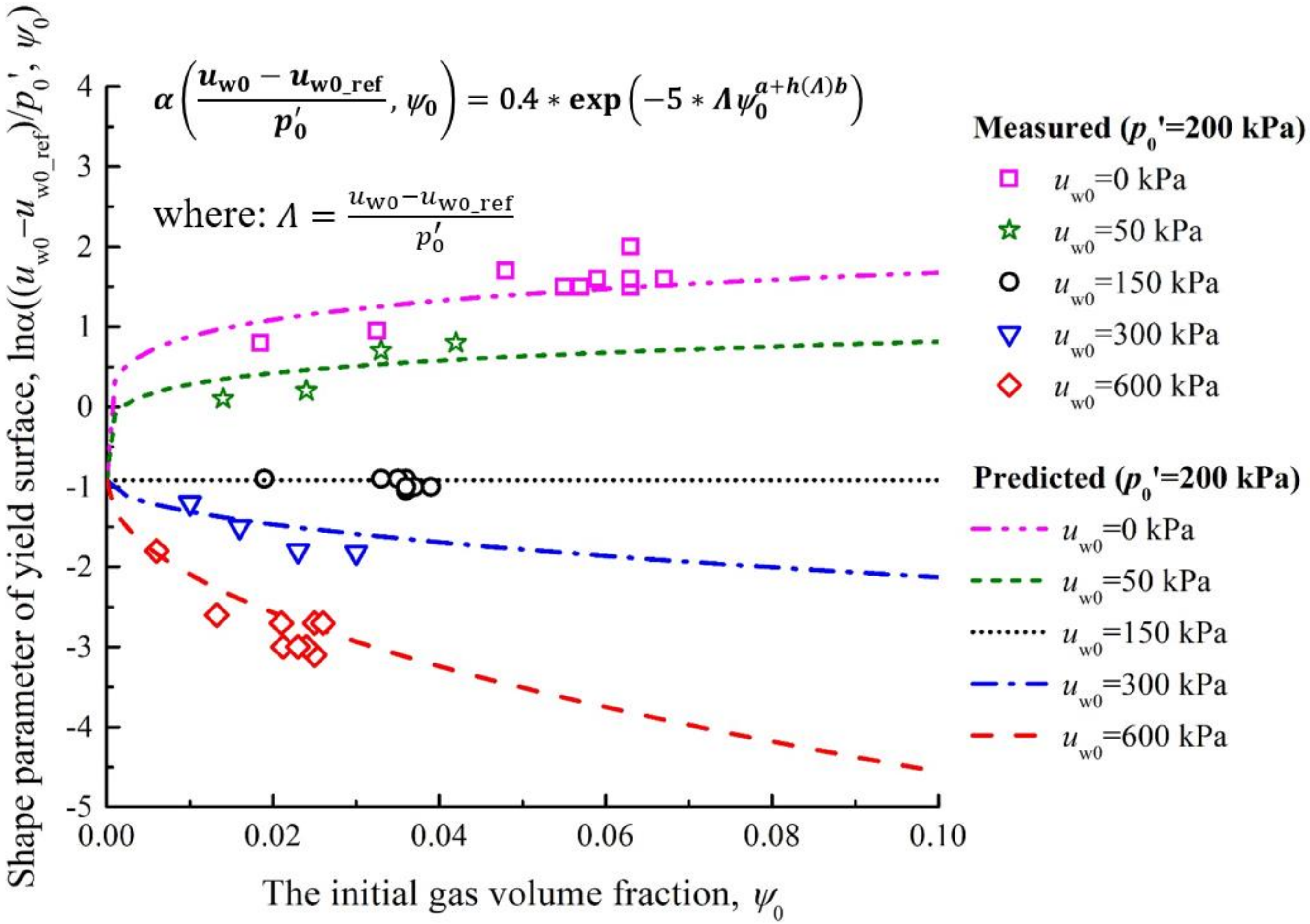

Fig. 8. Comparison between the measured and predicted shape parameter α for all the tests (in Series I and II).

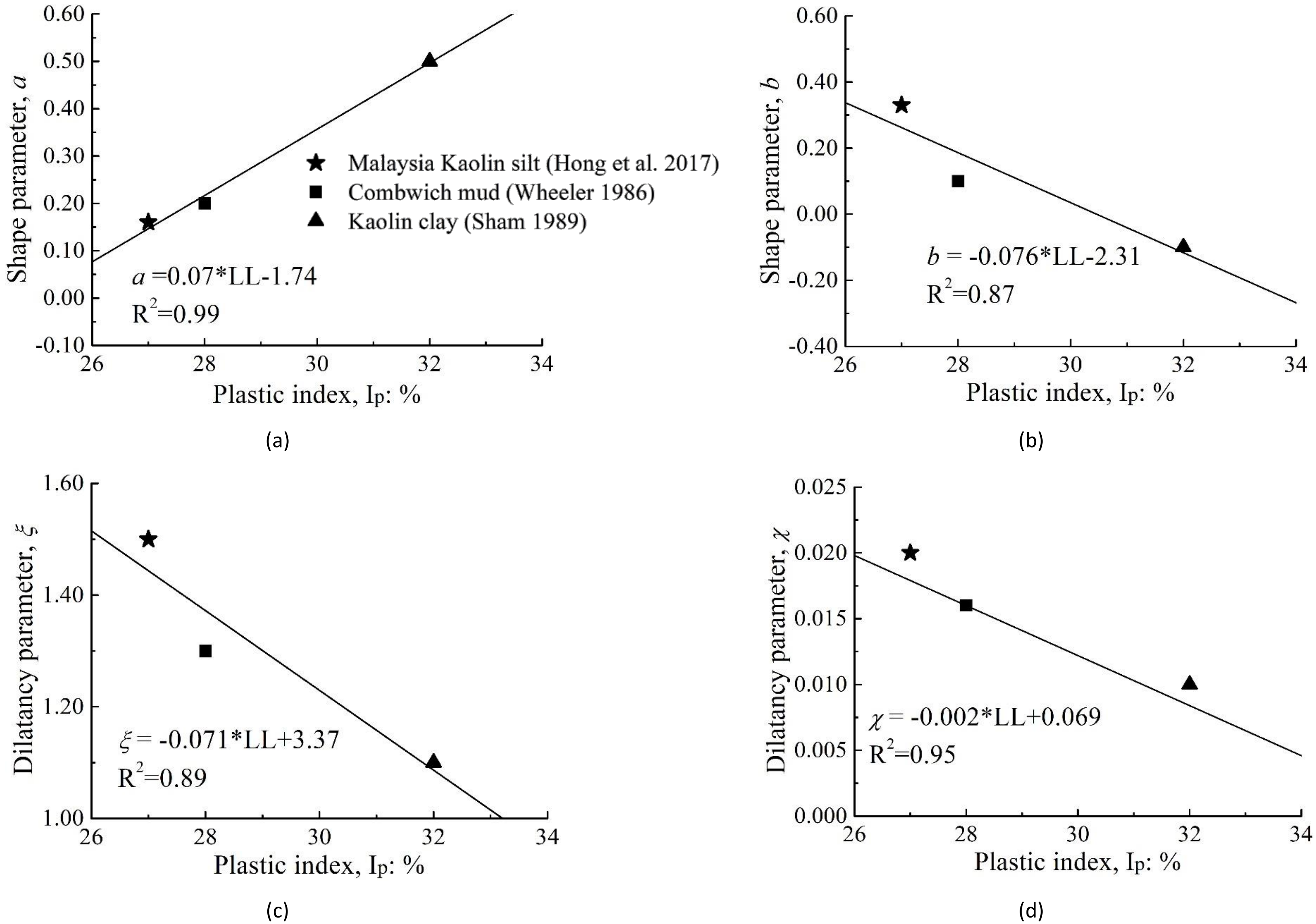

Fig. 9. Correlating the four new model parameters to the liquid limit (LL) of three types of fine-grained gassy soil.

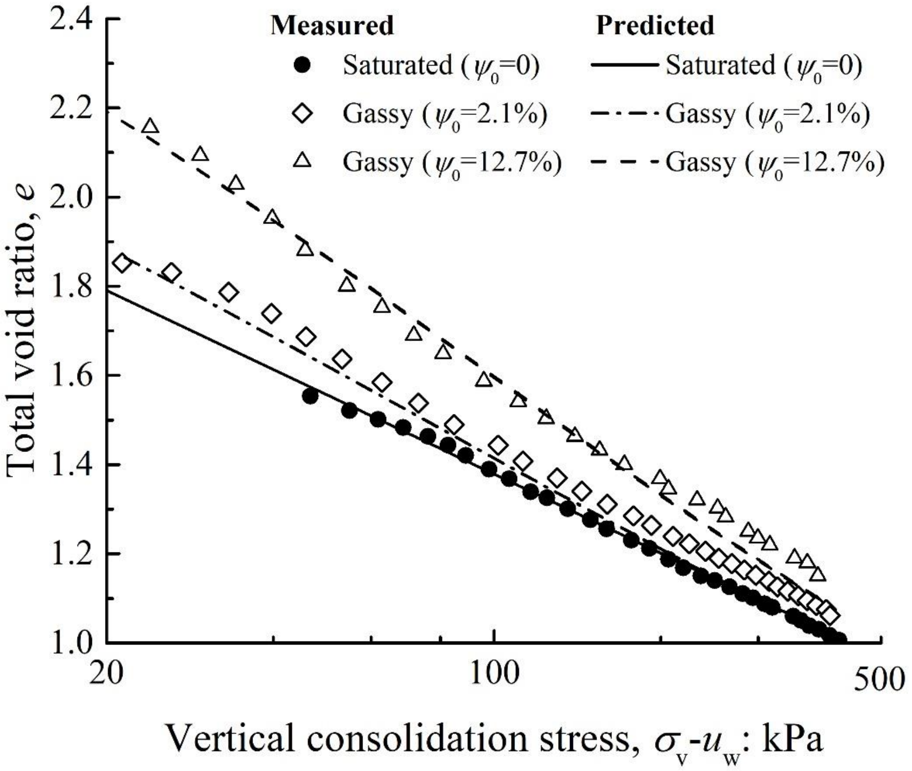

(a)

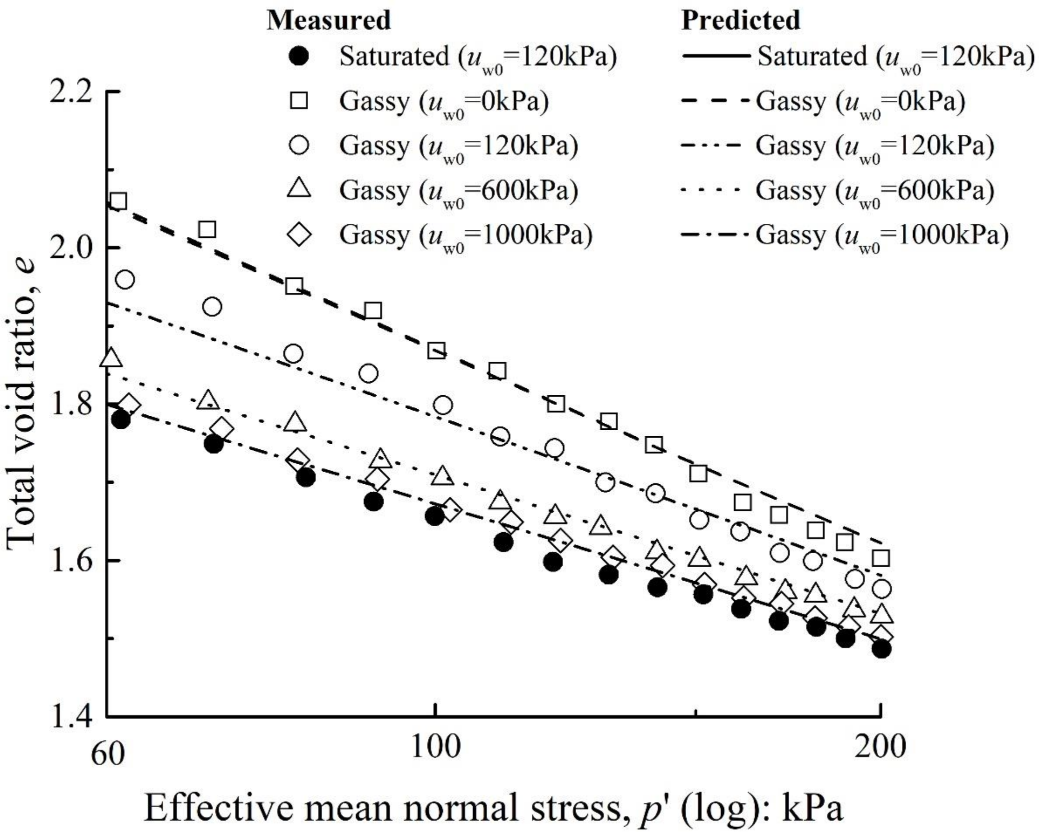

(b)

Fig. 10. Comparison between the predicted and measured compression behavior of (a) gassy Combwich

mud (data from Thomas 1987); (b) gassy Malaysia Kaolin silt (data from Hong et al. 2017).

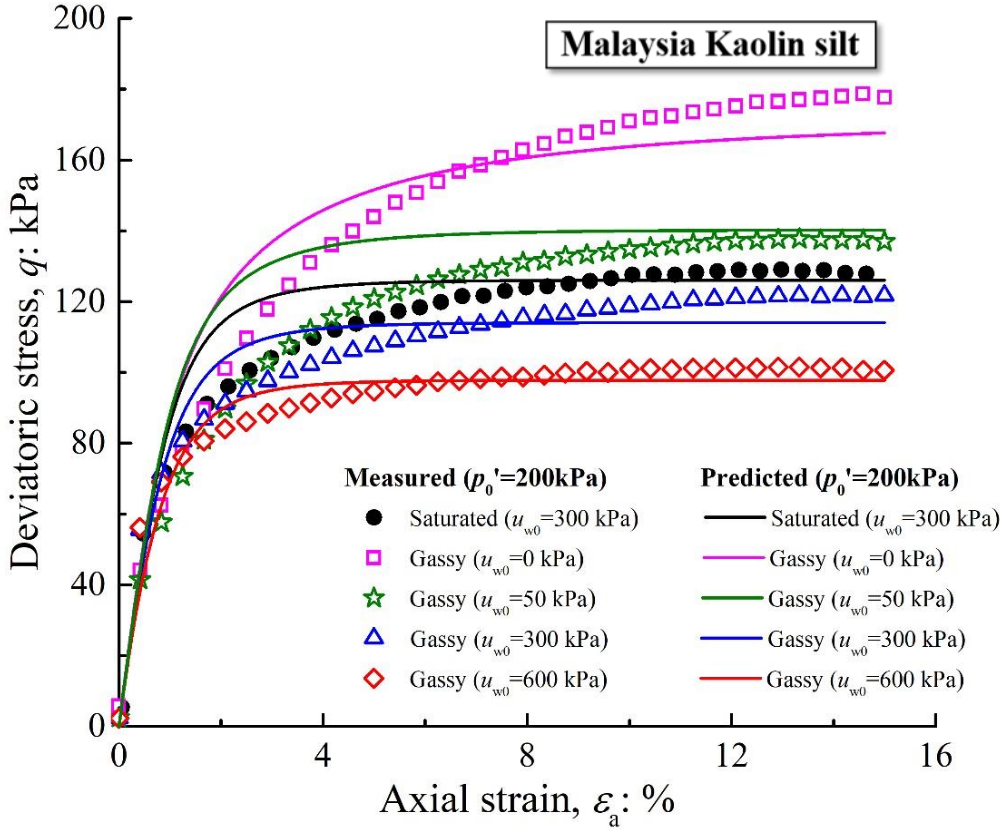

Malaysia Kaolin silt
Deviatoric stress, q: kPa
Axial strain, εa: %
Measured (p0'=200kPa)
Predicted (p0'=200kPa)
Saturated (uw0=300 kPa)
Gassy (uw0=0 kPa)
Gassy (uw0=50 kPa)
Gassy (uw0=300 kPa)
Gassy (uw0=600 kPa)

(a)

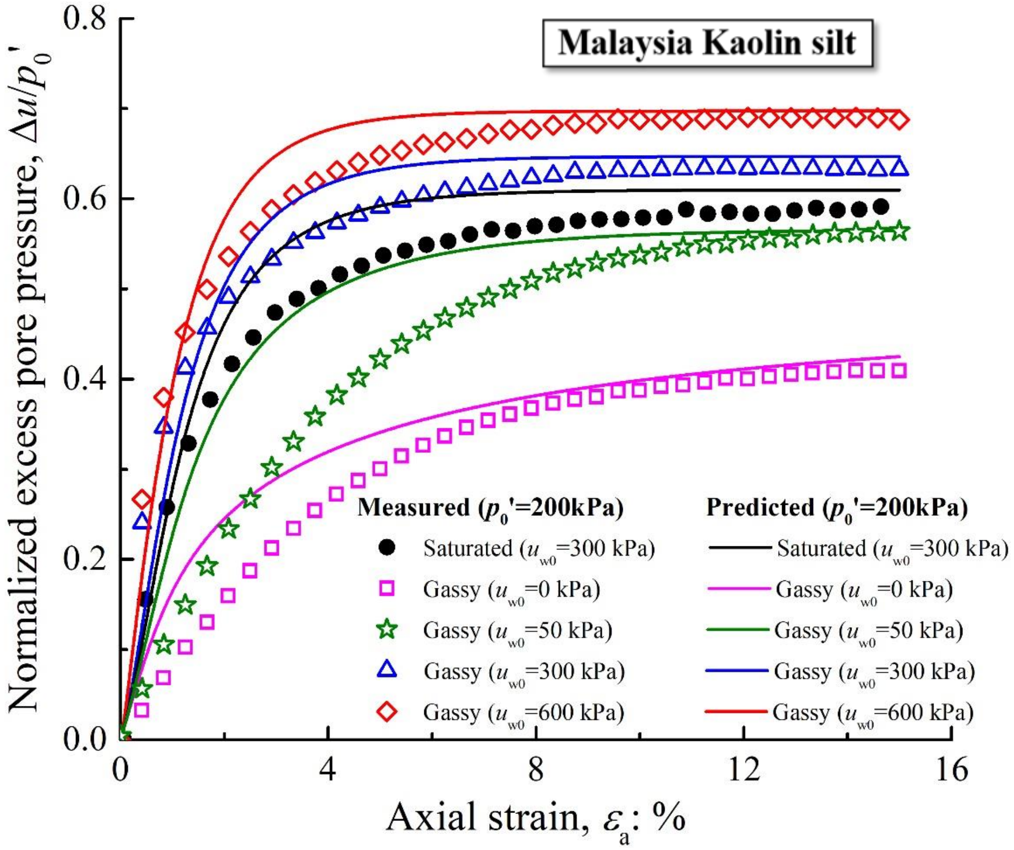

Malaysia Kaolin silt
Normalized excess pore pressure, Δu/p0'
Axial strain, εa: %
Measured (p0'=200kPa)
Predicted (p0'=200kPa)
Saturated (uw0=300 kPa)
Gassy (uw0=0 kPa)
Gassy (uw0=50 kPa)
Gassy (uw0=300 kPa)
Gassy (uw0=600 kPa)

(b)

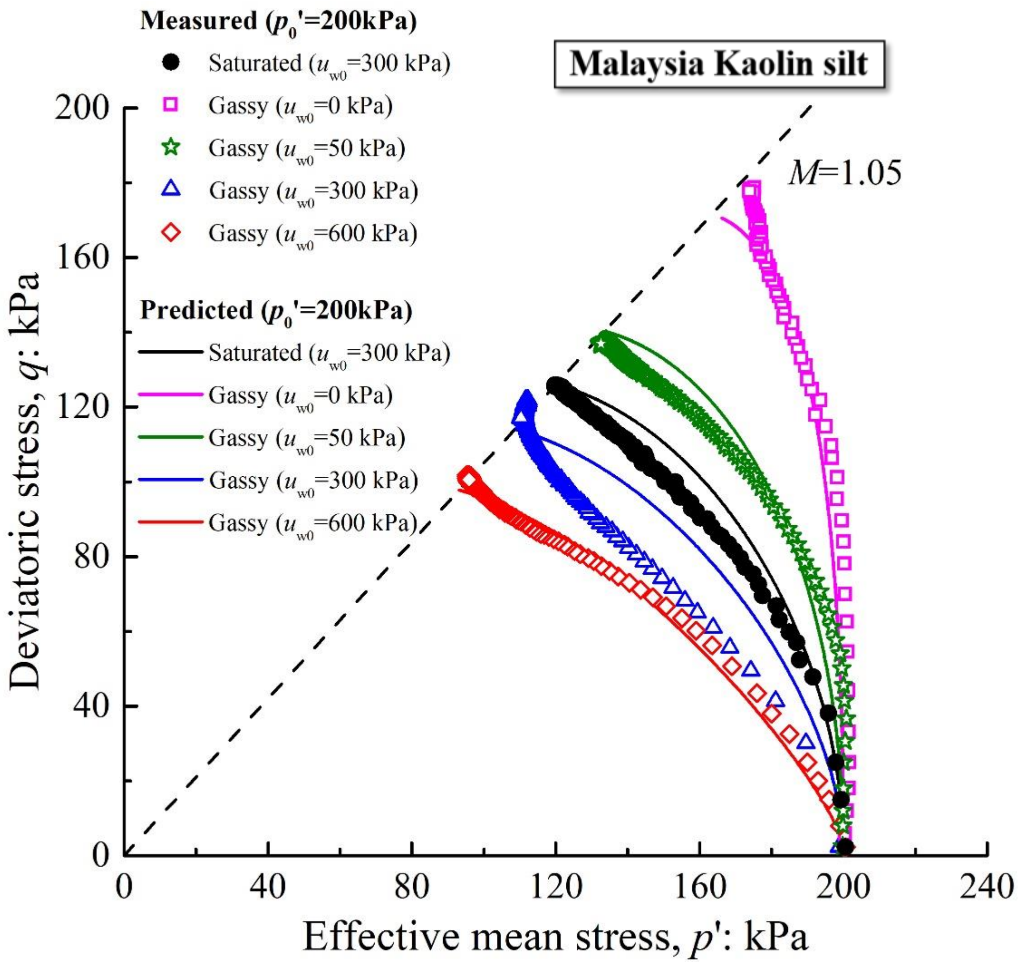

(c)

Fig. 11. Comparison between the predicted and measured shear behavior of gassy Malaysia Kaolin silt (data from Hong et al. 2019b): (a) stress-strain relation; (b) pore pressure response; (c) effective stress path.

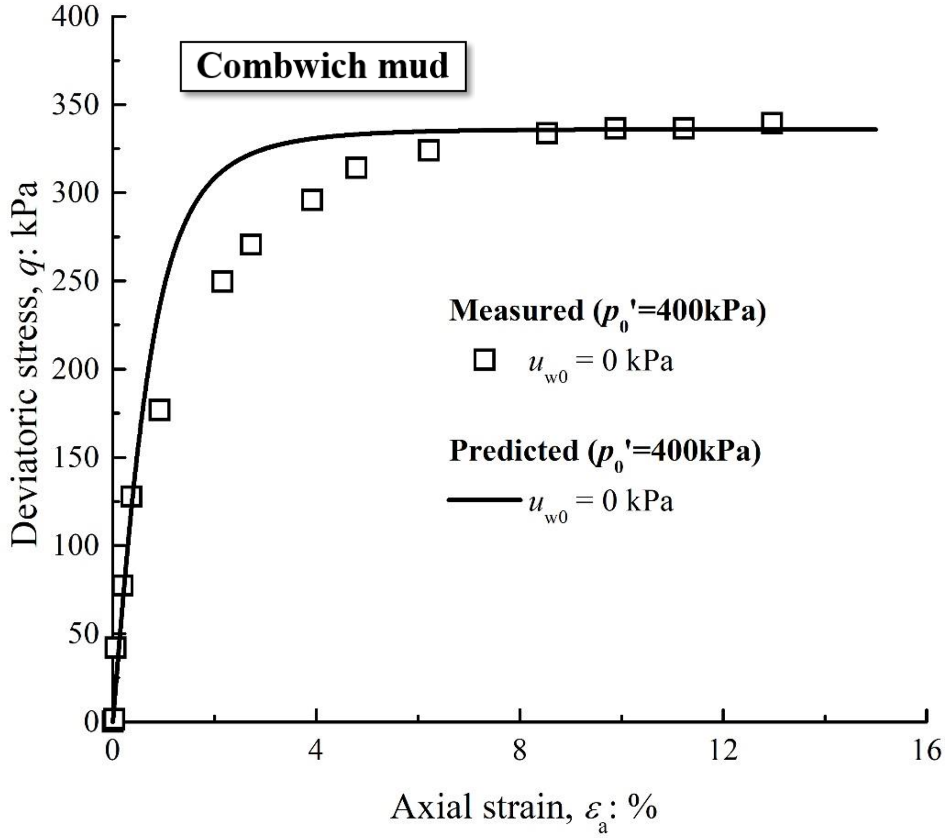

Combwich mud
Deviatoric stress, q: kPa
Axial strain, εa: %
Measured (p0'=400kPa)
uw0 = 0 kPa
Predicted (p0'=400kPa)
uw0 = 0 kPa

(a)

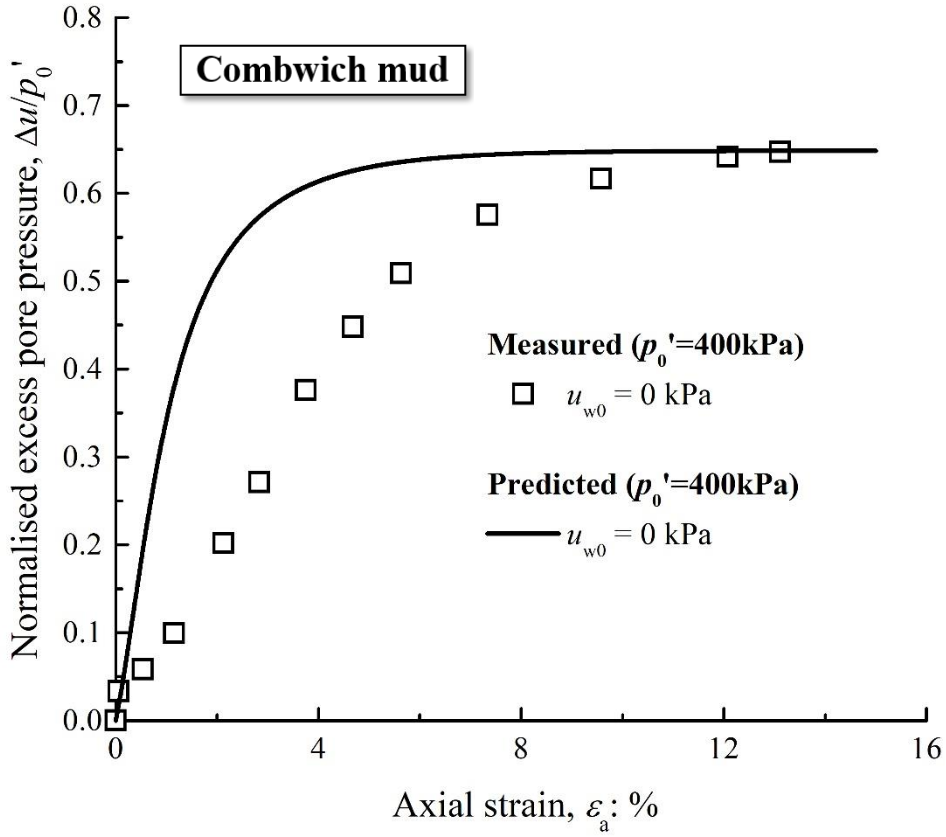

Combwich mud
Normalised excess pore pressure, Δu/p0'
Axial strain, εa: %
Measured (p0'=400kPa)
uw0 = 0 kPa
Predicted (p0'=400kPa)
uw0 = 0 kPa

(b)

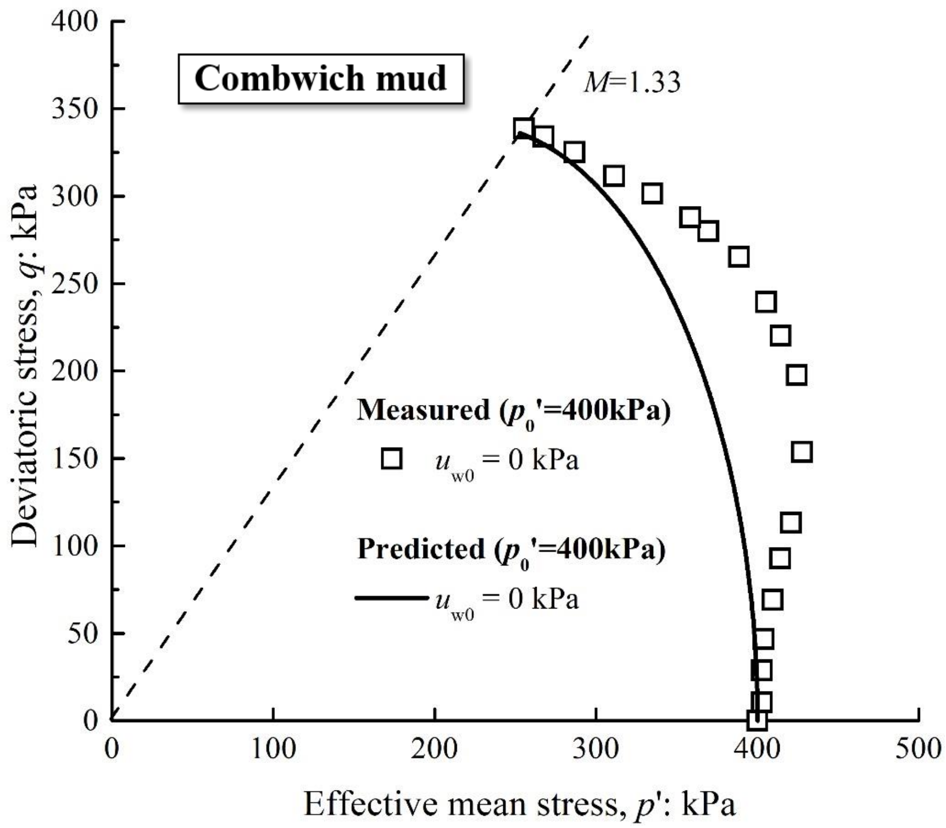

(c)

Fig. 12. Comparison between the predicted and measured shear behavior of gassy Combwich mud (data from Wheeler 1986): (a) stress-strain relation; (b) pore pressure response; (c) effective stress path.

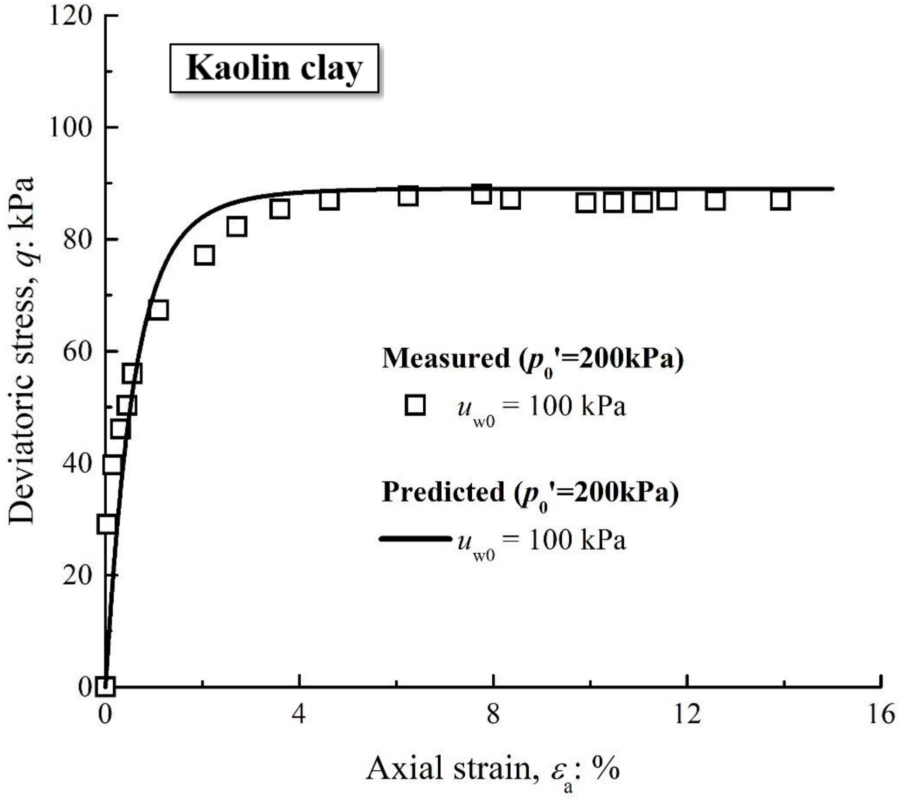

(a)

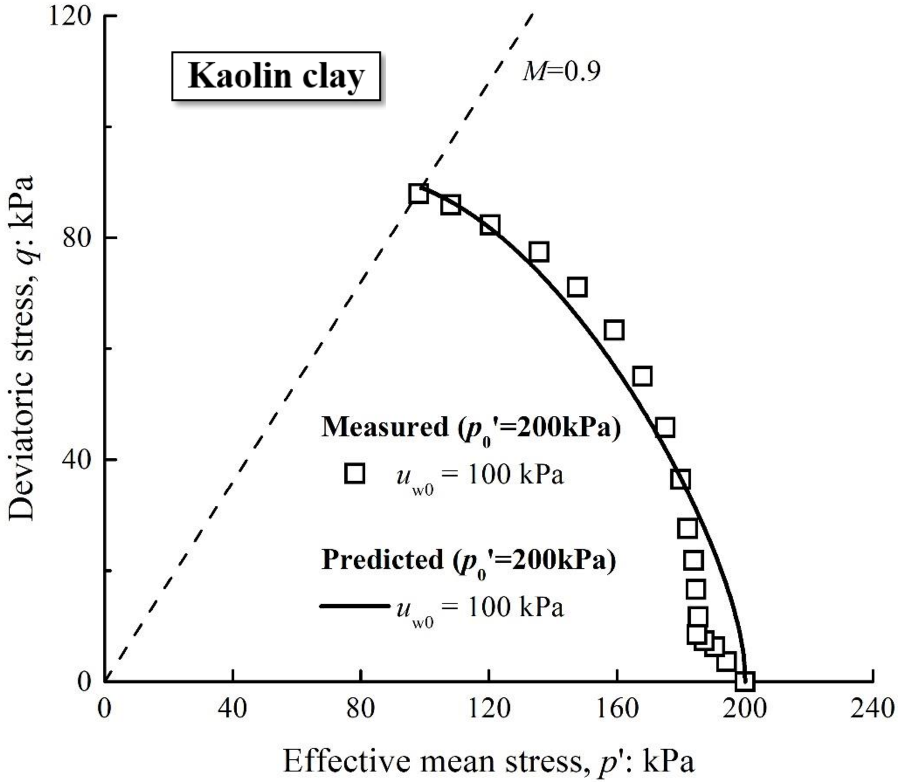

(b)

Fig. 13. Comparison between the predicted and measured shear behavior of gassy Kaolin clay (data from Sham 1989): (a) stress-strain relation; (b) effective stress path.

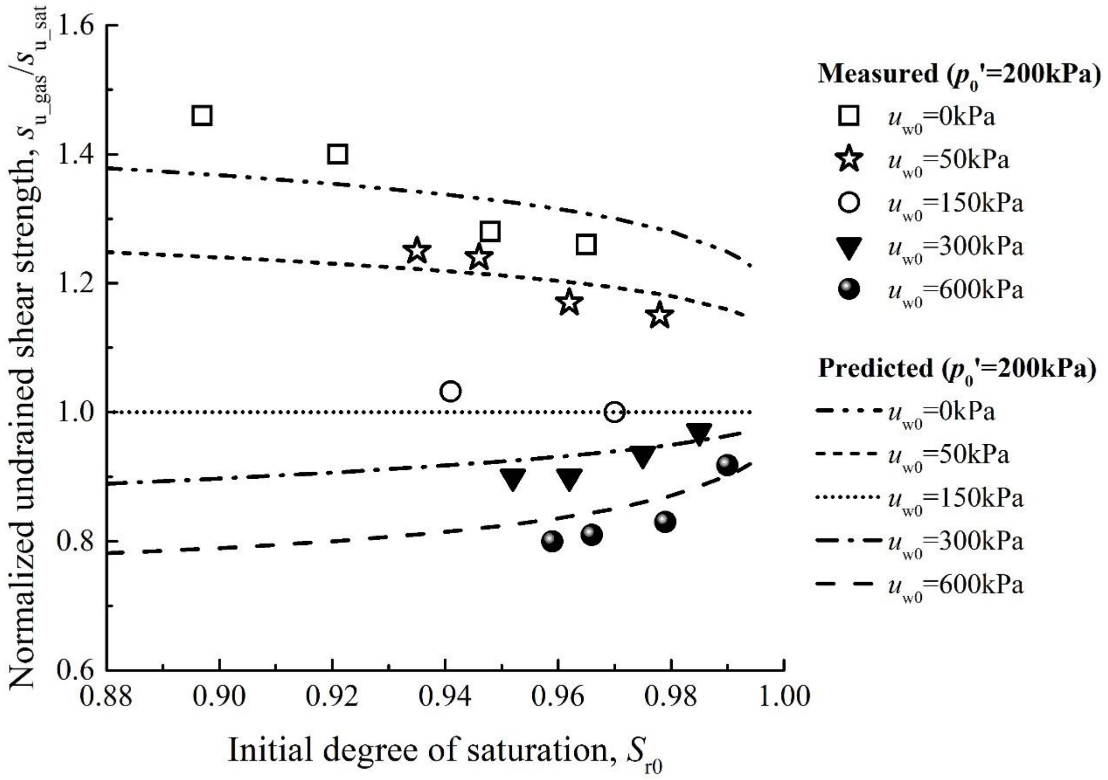

Fig. 14. Comparison between the predicted and measured undrained shear strength of gassy Malaysia Kaolin silt (data from Hong et al. 2019b).

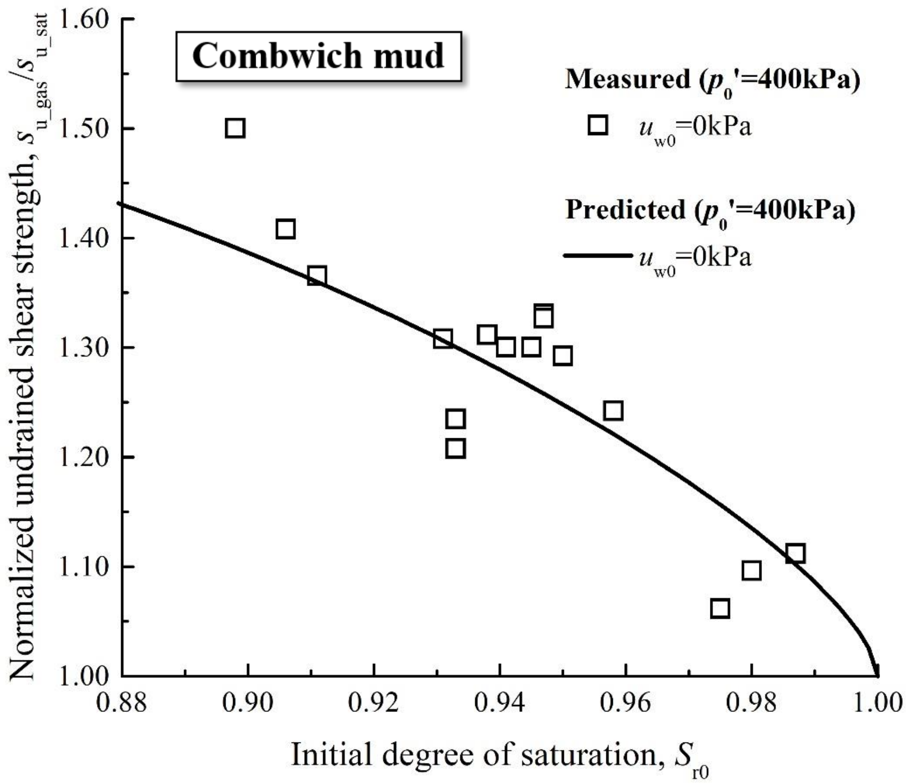

(a)

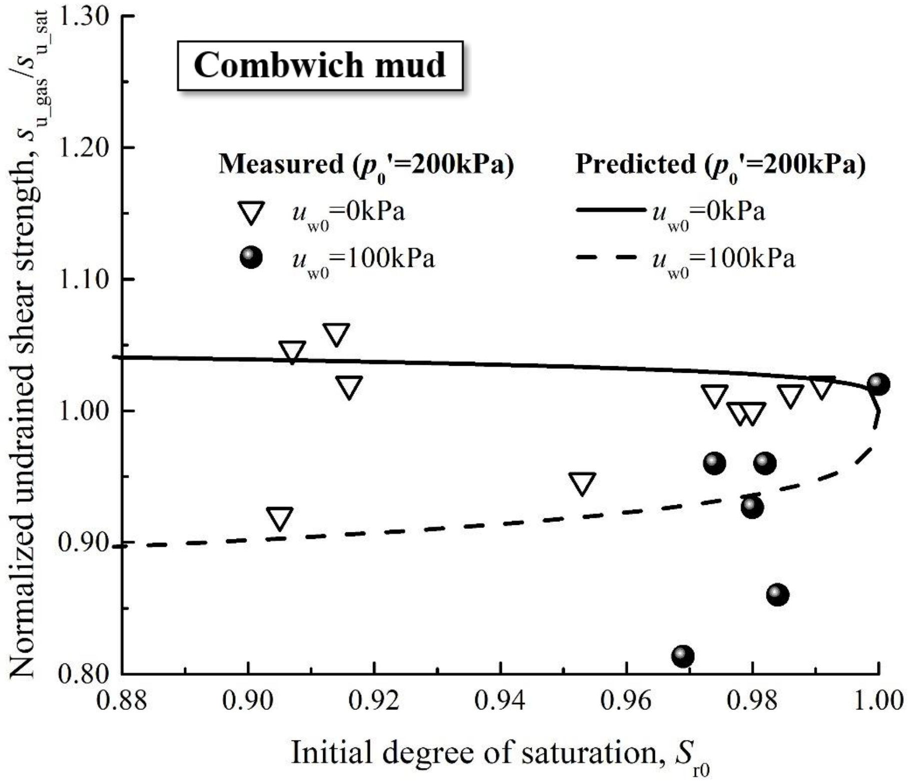

(b)

Fig. 15. Comparison between the predicted and measured undrained shear strength of gassy Combwich mud (data from Wheeler 1986).

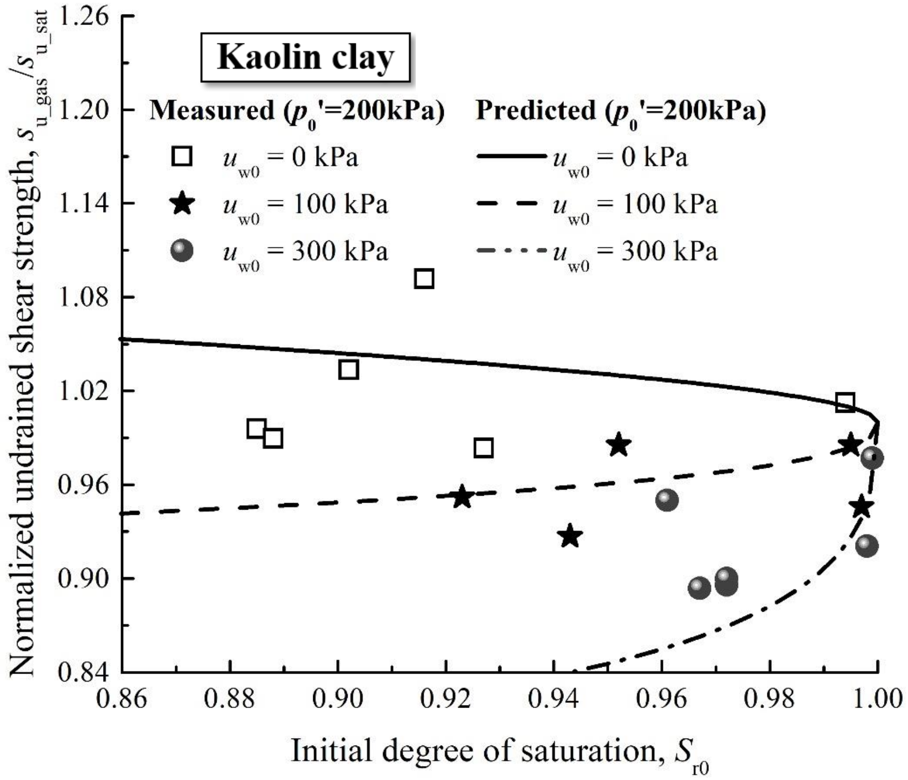

(a)

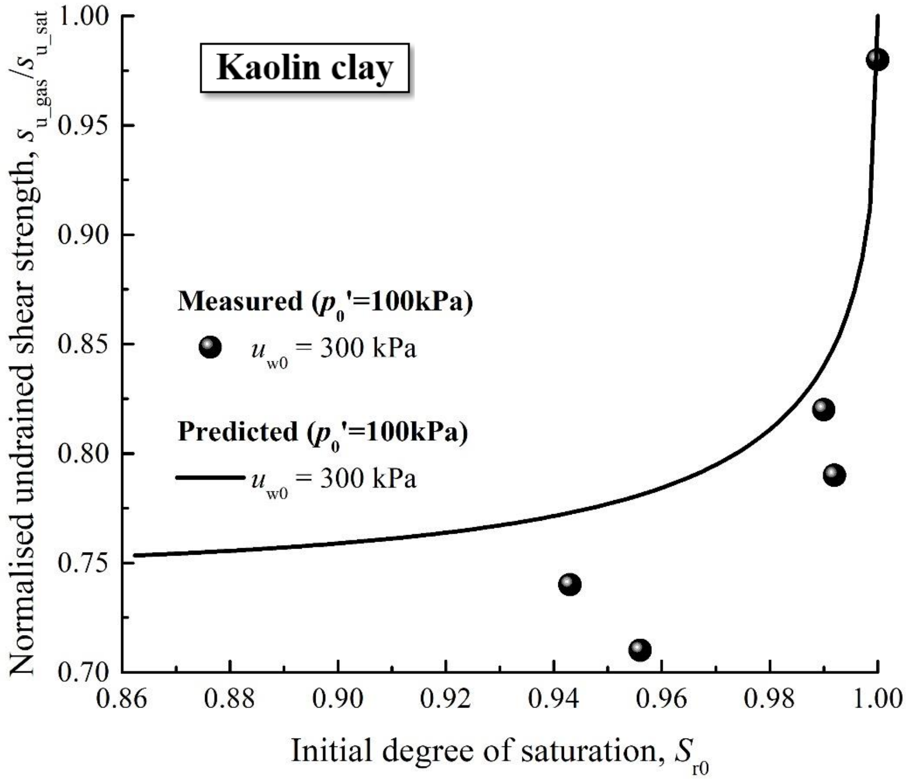

(b)

Fig. 16. Comparison between the predicted and measured undrained shear strength of gassy Kaolin clay (data from Sham 1989).

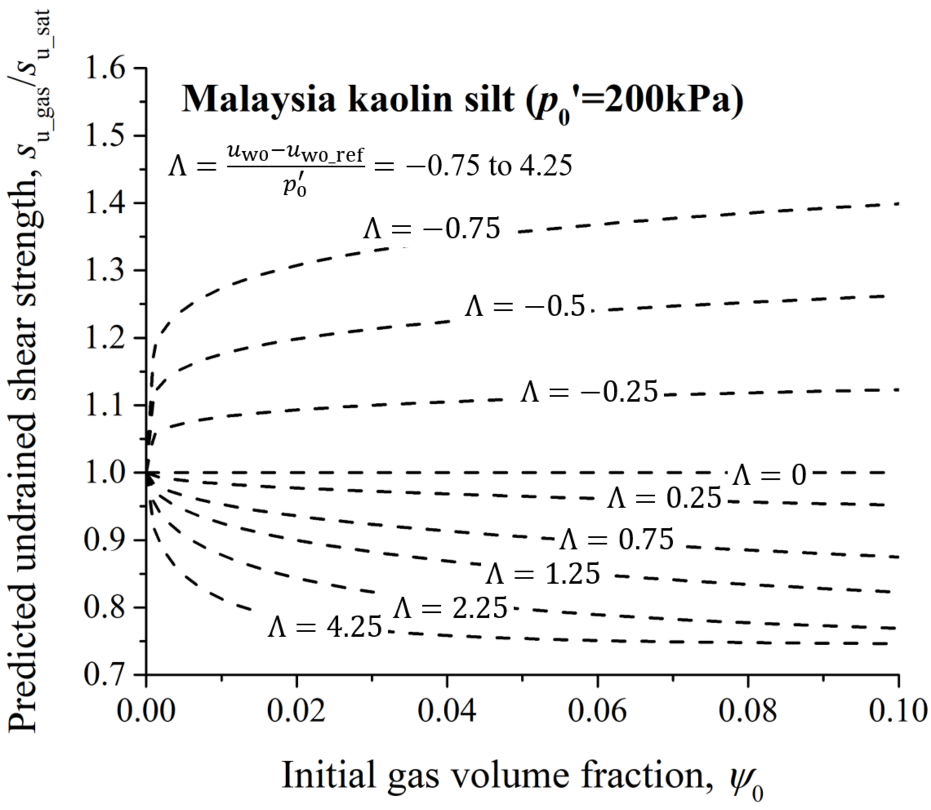
Malaysia kaolin silt (p_0'=200kPa)
$\Lambda = \frac{u_{wo} - u_{wo\_ref}}{p'_0} = -0.75$ to 4.25
$\Lambda = -0.75$
$\Lambda = -0.5$
$\Lambda = -0.25$
$\Lambda = 0$
$\Lambda = 0.25$
$\Lambda = 0.75$
$\Lambda = 1.25$
$\Lambda = 2.25$
$\Lambda = 4.25$
Predicted undrained shear strength, s_{u_gas}/s_{u_sat}
Initial gas volume fraction, ψ_0
1.6
1.5
1.4
1.3
1.2
1.1
1.0
0.9
0.8
0.7
0.00
0.02
0.04
0.06
0.08
0.10

(a)

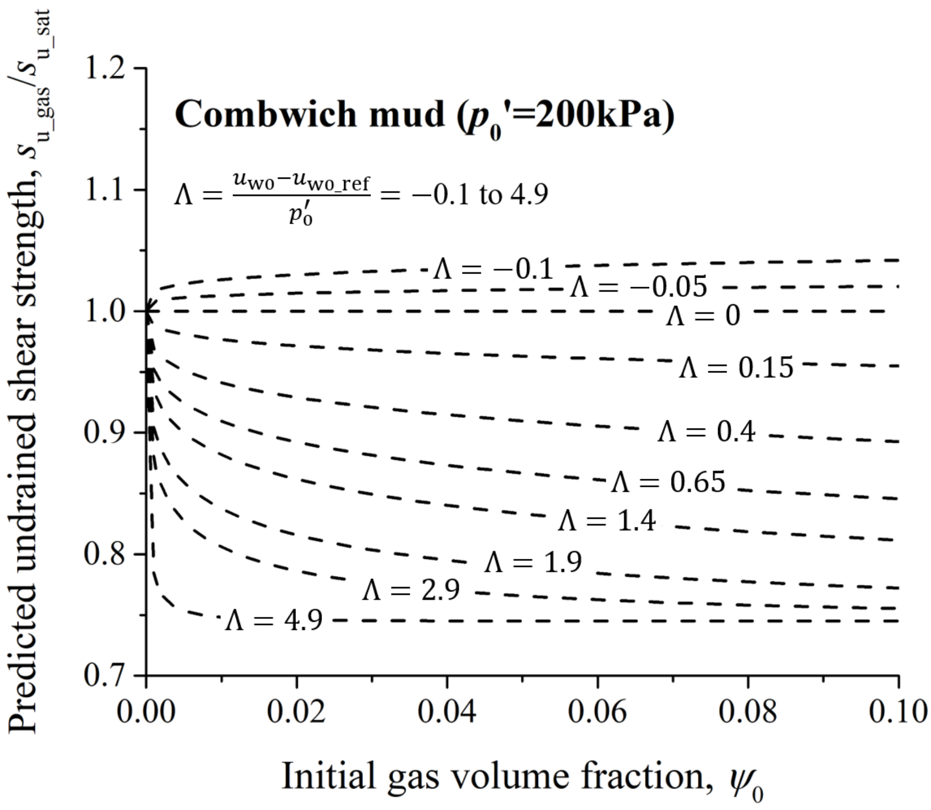
Combwich mud (p_0'=200kPa)
$\Lambda = \frac{u_{wo} - u_{wo\_ref}}{p'_0} = -0.1$ to 4.9
$\Lambda = -0.1$
$\Lambda = -0.05$
$\Lambda = 0$
$\Lambda = 0.15$
$\Lambda = 0.4$
$\Lambda = 0.65$
$\Lambda = 1.4$
$\Lambda = 1.9$
$\Lambda = 2.9$
$\Lambda = 4.9$
Predicted undrained shear strength, s_{u_gas}/s_{u_sat}
Initial gas volume fraction, ψ_0
1.2
1.1
1.0
0.9
0.8
0.7
0.00
0.02
0.04
0.06
0.08
0.10

(b)

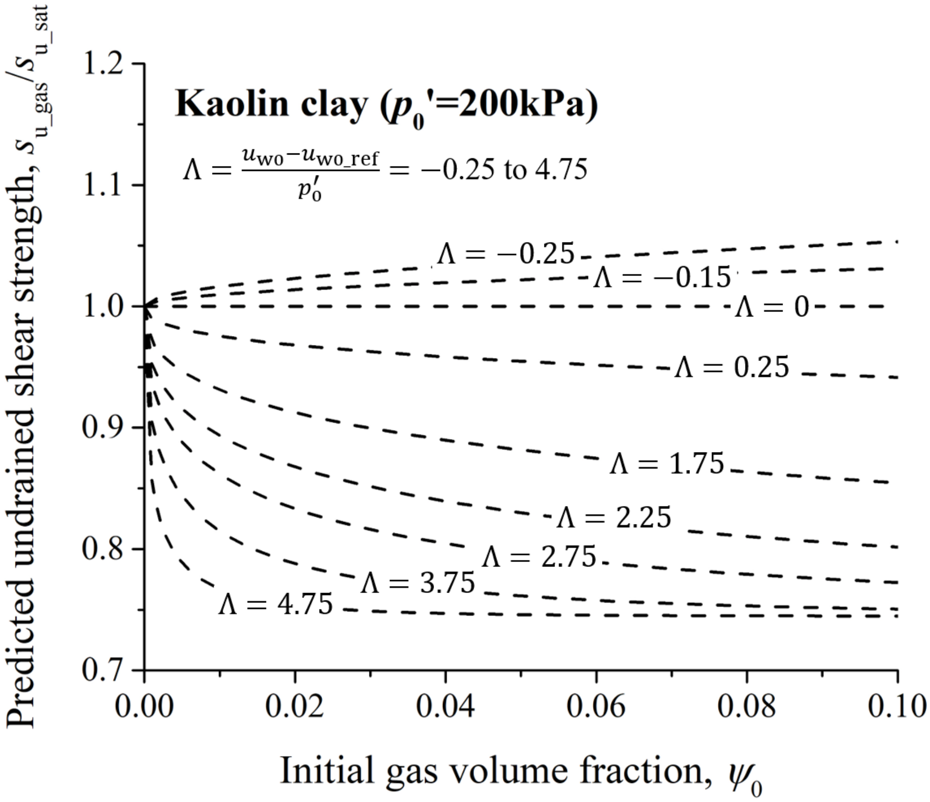

(c)

Fig. 17. Calculation chart for quantifying the s_u of gassy soils: (a) Malaysia kaolin silt; (b) Combwich mud; (c) Kaolin clay.